CONTRACT REPORT ARBRL-CR-00398

INTERIOR AND TERMINAL BALLISTICS OF 25g LONG ROD PENETRATORS

Prepared by

University of Dayton Research Institute
300 College Park Avenue
Dayton, Ohio 45469

April 1979

US ARMY ARMAMENT RESEARCH AND DEVELOPMENT COMMAND
BALLISTIC RESEARCH LABORATORY
ABERDEEN PROVING GROUND, MARYLAND

Destroy this report when it is no longer needed.
Do not return it to the originator.

Secondary distribution of this report by originating or sponsoring activity is prohibited.

Additional copies of this report may be obtained from the National Technical Information Service, U.S. Department of Commerce, Springfield, Virginia 22151.

The findings in this report are not to be construed as an official Department of the Army position, unless so designated by other authorized documents.

The use of trade names or manufacturers' names in this report does not constitute indorsement of any commercial product.

REPORT DOCUMENTATION PAGE

READ INSTRUCTIONS BEFORE COMPLETING FORM

1. REPORT NUMBER: CONTRACT REPORT ARBRL-CR-00398
2. GOVT ACCESSION NO.
3. RECIPIENT'S CATALOG NUMBER

4. TITLE (and Subtitle): INTERIOR AND TERMINAL BALLISTICS OF 25g LONG ROD PENETRATORS
5. TYPE OF REPORT & PERIOD COVERED: Final Report
6. PERFORMING ORG. REPORT NUMBER: UDR-TR-77-62

7. AUTHOR(s): Dr. Stephan J. Bless
8. CONTRACT OR GRANT NUMBER(s): DAAD05-76-C-0766

9. PERFORMING ORGANIZATION NAME AND ADDRESS:
University of Dayton Research Institute
300 College Park Avenue
Dayton, OH 45469

10. PROGRAM ELEMENT, PROJECT, TASK AREA & WORK UNIT NUMBERS

11. CONTROLLING OFFICE NAME AND ADDRESS:
US Army Ballistic Research Laboratory
ATTN: DRDAR-BLT
Aberdeen Proving Ground, MD 21005
12. REPORT DATE: APRIL 1979
13. NUMBER OF PAGES: 86

14. MONITORING AGENCY NAME & ADDRESS (if different from Controlling Office):
US Army Armament Research and Development Command
US Army Ballistic Research Laboratory
ATTN: DRDAR-BL
Aberdeen Proving Ground, MD 21005
15. SECURITY CLASS. (of this report): Unclassified
15a. DECLASSIFICATION/DOWNGRADING SCHEDULE

16. DISTRIBUTION STATEMENT (of this Report)

Approved for public release; distribution unlimited.

17. DISTRIBUTION STATEMENT (of the abstract entered in Block 20, if different from Report)

18. SUPPLEMENTARY NOTES

19. KEY WORDS (Continue on reverse side if necessary and identify by block number)

Terminal ballistics	vulnerability	behind-target effects
Rod penetrators	interior ballistics	fragments
Sabot	armor	lethality

20. ABSTRACT (Continue on reverse side if necessary and identify by block number)

Techniques were developed to launch 25g L/D=10 rods from a 50mm propellant gun. The rods were S-7 tool steel, W-Ni-Fe alloy, and Co-bonded WC. The velocities were in the range 1.8 to 2.58 km/s. The rods were launched against 25.4mm 4340 steel plates at 0° and 45° obliquity, and four 6.35mm 2024-T3 aluminum plates. Behind-target fragment data were obtained by flash x-ray analyses, witness plate measurements, and recovery of fragments.

FOREWORD

This document is the final report for work performed under Contract DAAD05-76-C-0766, for the U. S. Army Ballistic Research Laboratory. The Project Monitor was Mr. Graham Silsby. The Principal Investigator was Dr. Stephan Bless. Most of the firings were carried out by Messrs. Michael Nagy, Mark Nagy, and Edward Strader. Mr. Silsby of the BRL and Mr. Hallock F. Swift and Dr. John P. Barber of UDRI provided valuable technical comments during the program.

TABLE OF CONTENTS

LIST OF ILLUSTRATIONS

LIST OF ILLUSTRATIONS (continued)

LIST OF ILLUSTRATIONS (continued)

LIST OF TABLES

I. INTRODUCTION

This report concerns the perforation of metal plates by high-velocity rod penetrators. There has been a great deal of interest recently in the performance of such projectiles. The effectiveness of rod penetrators at conventional ordnance velocities (approximately 1.4 km/s) has been well documented, and several rod projectiles are either already in the inventory or in the final development stages[1]. Improvements in delivery systems offer promise of launch velocities well above 1.4 km/s. This effort was designed to provide a qualitative and quantitative extension of rod penetration data to these higher velocities.

Specifically, rods studied in this report had a length to diameter ratio, (L/D) of 10, and they are composed of AISI S-7 steel, tungsten alloy (W-alloy), and tungsten carbide (WC). The targets were steel and aluminum single and multiple plates. The launch velocities were between 1.8 and 2.6 km/s. The objectives of the experiments were (1) to identify effective penetrator materials, (2) to collect behind-target data, and (3) to generate an improved physical understanding of the penetrator process.

A. Background

The penetration mechanics of long rods at ballistic velocities has been a subject of intensive research during the past several years[1,2,3,4]. The studies have been of four types:

---

[1]Rubin, L., S. F. Frederick, E. G. Kendall, and P. J. Blatz, "An Overview of DoD Activities in Kinetic Energy Penetrator Technology Volume I: Activity Summaries" SAMSO-TR-76-187 (available SAMSO/YAPT, P. O. Box 92960, Worldway Postal Center, L. A., CA., 90009) August 1976.

[2]Rubin, L., S. F. Frederick, E. G. Kendall, and P. J. Blatz, "An Overview of FoD Activities in Kinetic Energy Penetrator Technology Volume II: Commentary" SAMSO-TR-76-187 (available SAMSO/YAPT, P. O. Box 92960, Worldway Postal Center, L.A., CA., 90009) August 1976.

[3]High Density Penetrator Materials Conference, U. S. Army Foreign Science and Technology Center, Charlottesville, VA., May 1976.

[4]"Ringers, B. E., and J. A. Zukas, "Numerical Simulation of Yawed Rod Impacts," BRL Memorandum Report in preparation, April 1979.

(a) collection of empirical data (unfortunately, many of these tests concerned particular penetrator designs and are of limited applicability.), (b) analysis of empirical results, (c) theoretical analysis of penetration phenomena, and (d) numerical simulation of penetration events.

The most numerous efforts have concerned penetration of single plates of armor. Data spanning many L/D ratios and penetrator materials are available[4,5,6,7]. It has been found that penetration is favored by high L/D ratio and high density. Some theoretical work has indicated that a hemispherical nose is essential for maximum penetration against hard targets[8,9]; the experimental evidence on this point is less clear[5]. Among the tested means of characterizing material properties, the unnotched Charpy energy appears to be the best indicator of penetration performance[7].

The effects of target obliquity may be taken into account, to first order, by considering the total line-of-sight target thickness[5], d sec θ (where θ is obliquity). A closer approximation, however, is obtained by using the quantity[10] d $(1 + 2 \sec \theta)/3$ as an equivalent thickness of plate at normal incidence.

---

[5]Grabarek, C. L., "Penetration of Armor by Steel and High Density Penetrators," BRL-MR-2134 (AD #518394L), October 1971.

[6]Nowak, S. P., and J. M. Katlin, "Ballistic Evaluation of Tungsten Materials as Penetrators Pertinent to 25-30 mm Weapons Systems," presented at meeting of reference 3.

[7]Bloore, E. W., "Penetrator Performance and Mechanical Properties," presented at meeting of reference 3.

[8]Norris, D. M., J. K. Scudder, W. H. McMaster, and M. L. Wilkins, "Mechanics of Long-Rod Penetration at High Angles of Obliquity," presented at meeting of reference 3, also UCRL-77941, May 1976.

[9]Jonas, G. H., "Theoretical Penetration Studies of Jacketed Steel Projectiles," BRL-MR-2654, August 1976. (AD #B013052L)

[10]Lambert, J. P., J. J. Misey, P. G. Morfogenis, and J. A. Zukas, "Behind Armor Data for Long Rod Penetrators," BRL-IMR No. 430, September 1975.

The effects of yaw on penetration are not well established. It has been proposed that a yaw angle of only a few degrees significantly degrades penetration ability[11,12]. However, other studies have found that for thick targets yaw angles of approximately 20° had relatively little affect on penetration[13,14].

The question of scaling has been recently examined by several investigators[5,16]. Unfortunately, a complete and rigorous evaluation of linear replica scaling* does not yet appear to be available. However, data reported in References 5, 15, and 16 do suggest that for metal projectiles and targets, linear scaling would be essentially fulfilled if material differences and imperfections in impact geometry could be avoided.

Theoretical and empirical formulas for describing target penetration have a long history. Unfortunately, in the velocity regime of concern here, it is particularly difficult to treat steel because strength effects cannot be neglected. Among the important physical processes which take place during penetration are

---

[11]Herr, E. L., and C. Grabarek, "Establishment of Standards for Penetrator Performance," presented in meeting of reference 3.

[12]Grabarek, C., "Methods of Data Acquisition and Presentation for Kinetic Energy Penetrators," Presented at the JTCG/ME Working Party for Kinetic Energy Penetrators, Information Exchange Meeting, 13-14 February 1973. U. S. Army Ballistic Research Laboratories, Aberdeen Proving Ground, Maryland.

[13]Bless, S. J., and R. S. Bertke, "Impact of Yawed Rods on Armor Plate," UDRI-TR-76-19, Final Report Contract No. DAAD05-74-C-0728, BRL, August 1976.

[14]Bertke, R. S., J. F. Heyda, H. F. Swift, and M. F. Lehman, "A Study of Yawed Rod Impacts," BRL-CR-182, October 1974. (AD #B000849L)

[15]Baker, E. E., and A. S. Westine, "Model Analysis for Penetration of Spaced Armor," BRL-CR-327, January 1977. (AD #A035460)

[16]Williams, A. E., "Impact Tests with Massive Short Rods," NRL Washington, DC 20378, paper presented at Twenty-Seventh Meeting Aeroballistic Range Association, Sevran, France 1976.

*By linear replica scaling we mean the following: If distances and times are multiplied by a constant scale factor, then at corresponding distances and times, velocity and stress have the same values.

- compressive failure of target and projectile material
- radial flow of projectile material
- axial deceleration and flow of projectile material
- radial and axial acceleration and plastic flow of target material
- tensile failure and spallation of target material

No current theory includes all of these effects. Projectile failure and spall formation seem to be the processes most resistant to theoretical analysis. However, theoretical treatments of several of the other processes have yielded valuable insights.

Recht and Ipson[17] showed the frequently observed $V_S - V_R$ relationship:

$$V_R^2 = \frac{M_p}{M_p + M_{plug}} (V_s^2 - V_L^2) \qquad (1)$$

can be explained by shear work done on the target*. Their analysis has been expanded to include target acceleration and flow[18,19]. However, due to projectile breakup, these theories become progressively more inaccurate as impact velocities exceed 1.5 km/s. If the impact velocity is high enough or the projectile strength is low enough, the penetration may be described by the hydrodynamic approximation[12,20]. In this limit, projectile velocity only weakly affects penetration.

---

[17]Recht, R. F., and T. W. Ipson, "Ballistic Perforation Dynamics," Trans ASME, September 1963, pp 384-390.

*In equation (1) and elsewhere, these symbols have their usual meaning; i.e., V and M are velocity and mass, while p, R, and L refer respectively to incoming projectile, principal behind-target fragment, and ballistic limit. Plug refers to any plug of target material ejected by the projectile.

[18]Goldsmith, E., and S. A. Finnegan, "Penetration and Perforation Processes in Metal Targets at and Above Ballistic Velocities," Int. J. Mech. Sci., 13, 843-866, 1971.

[19]Awerbach, J., and S. R. Bodner, "Analysis of the Mechanics of Perforation of Projectiles in Metallic Plates," Int. J. Solids 10, 671-684, 1974.

[20]Allen, W. A., and J. W. Rogers, "Penetration of a Rod into a Semi-Infinite Target," J. Franklin Inst., 272, 275-184, 1961.

A great many quasi-empirical or empirical penetration formulas have been proposed. For present purposes, the most useful of these is the generalized V_S-V_R-V_L relationship proposed by Lambert and Jonas[21].

$$V_R = \alpha(V_S^p - V_L^p)^{1/p} \qquad V_S > V_L$$
$$V_R = 0, \qquad V_S \leq V_L \tag{2}$$

For example, for L/D = 10 S-7 steel projectiles striking RHA* targets, the parameter p in five test series had a value of 2.56 with a standard deviation of 0.38.

Perforation of multiple-plate targets is much more difficult to achieve and to analyze than perforation of equivalent weight single-plate targets. Such targets may defeat a rod penetrator by causing it to deform or fragment, or by causing it to yaw as it travels between plates, especially in oblique impacts.

The factors which influence the effectiveness of penetrator materials against multiple targets are yet to be identified. Fracture toughness of the rod, at least, is of primary importance[7,22]. High strain rate and high temperature processes may also be important. In any case, it is evident that penetration capability is a very sensitive function of heat treatment and material constitution. For example, S-7 tool steel has been found to have batch-dependent penetration characteristics[23].

B. Outline of the Program

The research reported herein was designed to investigate penetration and target perforation in the velocity region above that normally used in rod penetration experiments. The targets were 25.4 mm thick steel at 0° and 45° obliquity, and four 6.35 mm aluminum plates at 0° obliquity. The impact velocities were between 1.8 km/s and 2.3 km/s. The projectile geometry and mass were kept constant: L/D = 10, hemispherically nosed 25 g rods. The rod materials were S-7 tool steel (Bethlehem's

---

[21]Lambert, J. P., and G. H. Jonas, "Towards Standardization in Terminal Ballistics Testing: Velocity Representation," BRL R 1852, January 1976. (AD #A021389)

[22]Katlin, J. M., and S. P. Nowak, "Scale Model High Density Penetrator Studies Simulating the 105 mm XM735 Projectile," paper presented at meeting of reference 3.

[23]Silsby, G. F., Private Communication, 1977.

*Rolled Homogeneous Armor.

"Bearcat" trademark steel), bonded WC, and a sintered/cemented WA penetrator material. Within this framework, the principal objectives of the research program were as follows:

- Develop techniques to launch laboratory-scale high-velocity rod penetrators with a propellant gun.
- Determine the important physical processes which occur during high-velocity rod penetration.
- Obtain behind-target data for high-velocity rod impacts and compare them with extrapolations of low-velocity results.
- Compare the relative performance of the three penetrator materials against steel armor and aircraft-type targets.

II. EXPERIMENTAL TECHNIQUE

The experiments were carried out on one of the ballistic ranges situated on the campus of the University of Dayton. The first portion of the program was devoted to the development of launch techniques for small high aspect ratio rods to velocities exceeding 1.5 km/s. This task involved considerable effort.

A. Ballistic Range

The range used for the experiments consisted of a 50mm propellant gun, two or three sections of blast tankage, a target impact chamber, and a projectile/fragment stopping system. Flash x-ray pictures of the projectile prior to impact and the behind-target fragments were made in the target chamber.

The launch tube consisted of two 3m long barrels connected end-to-end by a turnbuckle fastener. A seal ring prevented gas leakage at the joint, and provision was made to align the bores to within 0.03mm. The bore of the downrange tube was beveled slightly at its rear end to assure that no positive step would be encountered by a projectile. A metallic seal was used on the breech. The breech contained a chamber into which up to 1,300 g of propellants could be loaded through a rear opening. This opening was closed by a sleeve section containing a 50 mm diameter (bore diameter) hole aligned with the bore of the launch tube. This hole, in turn, was closed by a short piston which provided the rear face of the powder chamber at one end and bore against a 1,000 kg steel block at the other end. Upon firing, the high-pressure propellant gas acted upon both the base of the projectile and the face of the piston in such a way that no net momentum was transferred to the breech or the launch tube. The projectile was accelerated forward while the piston and recoil block were propelled rearward at relatively low velocities (typically, 0.02 percent of the projectile velocity). The steel block was brought to rest by a hydraulic shock absorber before it had moved 6.5 cm, and the length of the recoiling piston was adjusted so that its front face still closed the powder chamber when the motion of the steel block was terminated. Figure 1 provides a drawing of the gun. The pressure in the breech was monitored by means of a 700 MN/m^2 (1000 ksi) pressure transducer. Typical records for high and low performance shots are shown in Figure 2.

In the early stages of this program, the 50 mm launch tube was replaced with a smooth bore, 20 mm diameter, 5 m long tube. An appropriate nonrecoilless breech with a propellant capacity of 110 g was used.

Three blast tank sections were used in the main test series. The flight distance through these tanks was a little over 4 m. There are two interior baffles. The combined volume of the tanks was about 1 m^3. The blast tanks could be evacuated by means of 38 ℓ/s (60 ft^3/min) pump.

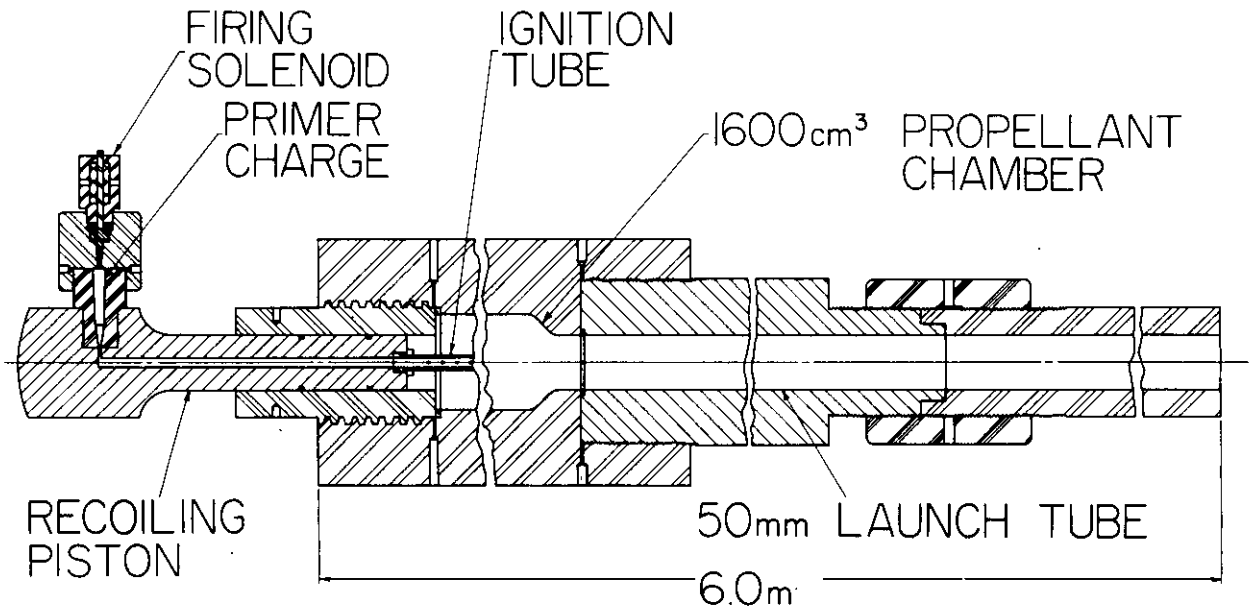

Figure 1. Cross Section Drawing of 50 mm Propellant Gun.

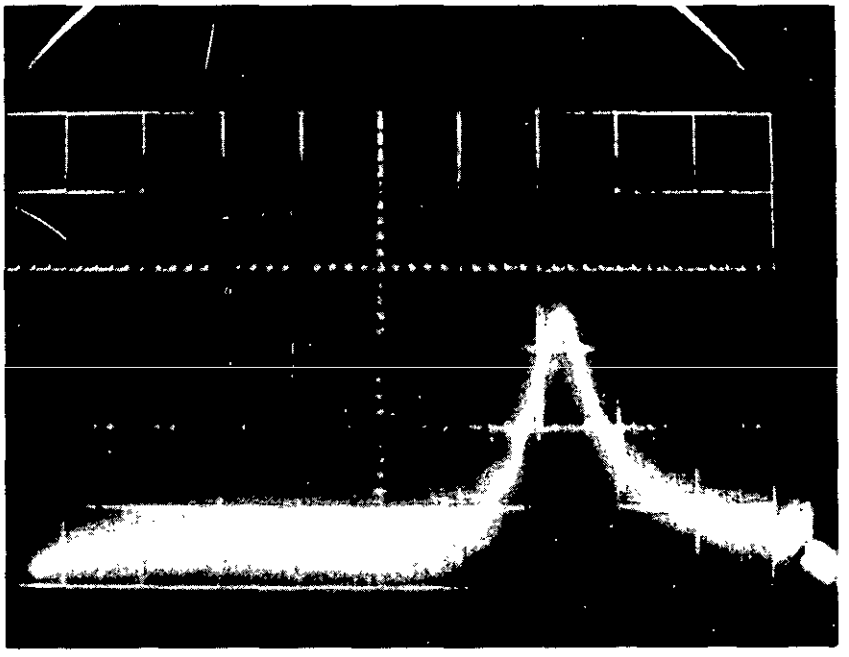

a. 630 g charge. 66 MN/m^2/div. 2 ms/div.

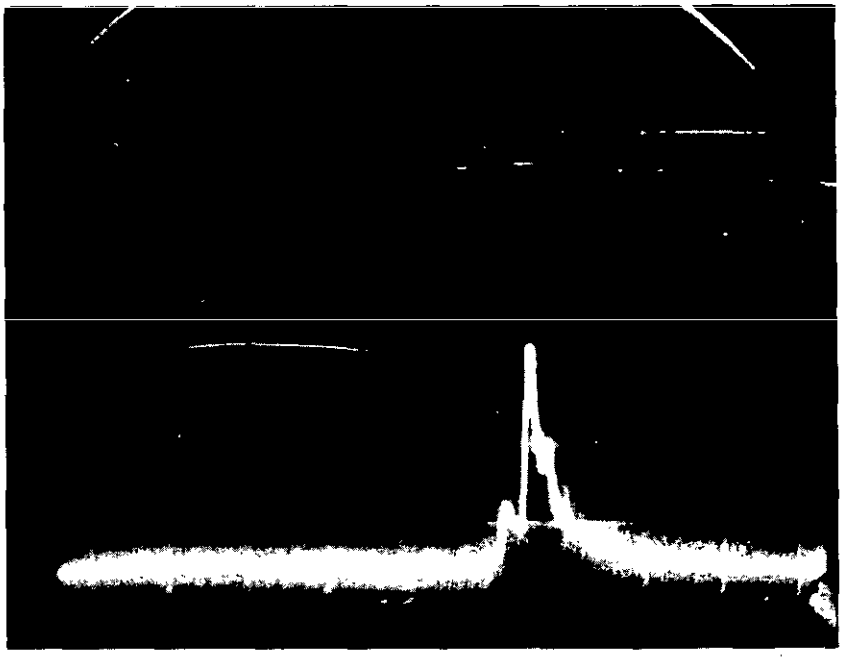

b. 1000 g charge. 263 MN/m^2/div. 2 ms/div.

Figure 2. Samples of pressure transducer data from breech of 50 mm gun

The target tank used in this program was especially designed for behind-target radiographs. It is shown (connected to two blast tank sections) in Figure 3. It was 110 cm long, and was constructed of 25 mm thick steel frame with 19 mm thick aluminum walls. The windows were vacuum sealed and consisted of 19 mm plexiglass. They were also often protected with 15 mm of 0.75 g/cm^3 particle board. A center baffle contained the vacuum seal (a Mylar* disc) for the preceding range elements. The target was mounted on studs fastened to massive support brackets 79 cm downrange from the face of the tank. The flash x-ray heads and film cassettes were all mounted on exterior attachments to the target tank.

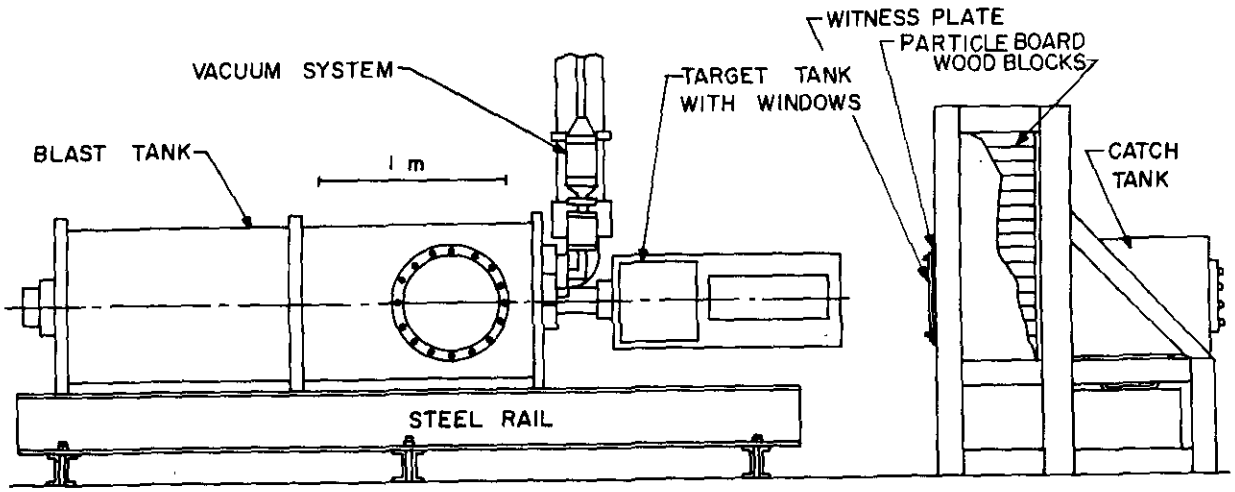

Figure 3. Sketch of two blast tank sections, target tank, and catcher assembly.

The target tank generally performed satisfactorily, but some improvements in design were suggested by our experiences. It would have been convenient to have been able to extend the field of view behind the target and to further separate the behind-target x-ray stations. In one shot, the windows blew out and damaged several x-ray tubes.

The projectile/fragment catching array was situated behind the target chamber. It is also shown in Figure 3. A 0.5 mm thick 0.44 m x 0.45 m 2024-T3 aluminum witness plate was located about 0.7 m behind the target mounting bracket (e.g., 0.7 m behind the impact surface of zero degree obliquity targets). The witness plates were attached with small stand-offs, onto two

*Mylar is a registered trademark of the E. I. duPont de Nemours and Company, Inc. for a polyester film.

pieces of particle board. The dimensions of the particle board varied somewhat, but the first was generally 0.62 m x 0.62 m, and the second was 0.62 m x 1.24 m (with the longer dimension horizontal). The thickness and density of the particle board is discussed in Section IV. Behind the particle board was a 0.9 m x 0.9 m x 0.3 m thick array of pine blocks with the end grain exposed. The individual blocks were 39 mm x 85 mm x 300 mm and were usually arranged so that fragments hit them on a smaller face. The wood blocks were backed by 20 mm of plywood, and behind the plywood was a large tank filled with sand.

In most experiments, only the principal fragment penetrated the particle board and entered the sand tank. Other fragments were caught in the particle board or block array.

The instrumentation of the target chamber consisted of eight channels of 180 kV flash x-rays, arranged in four orthogonal pairs. The first two pairs viewed the rod prior to impact, and the second two viewed the behind-target debris. The first pair were usually triggered from a twisted wire switch, which was found to be more reliable than a foil switch for use in a vacuum. The others were triggered from foil switches. The typical distances from the film planes to the trajectory, and from the trajectory to the x-ray heads, were 250 mm and 575 mm, respectively. The time interval between x-ray exposures was measured with digital counters.

The analysis of the radiographs was accomplished by use of an analog construction. Contact prints made from the four behind-target radiographs from a shot were mounted in the structure. The witness plate and particle boards were also mounted, and locations corresponding to the exit hole on the target and the x-ray sources were identified. Nylon string was strung from these locations to perforations of the particle board and images on the radiograph, respectively. Individual fragments which resulted in particle board perforation could thus be identified. (It was found that intuition was very unreliable for identifying corresponding images on the radiographs). The intersection points of the trajectory string with the strings between the sources and images defined the distance that the particles moved between exposures. This was used to calculate particle velocity vectors.

B. Penetrator Materials

The S-7 tool steel rods were made from drill rods purchased from Time Steel Service (Cleveland, Ohio). The manufacturer was Bethlehem Steel. The rods were heat treated to a hardness of Rockwell C-55 ± 1. Representative rods were examined by the wet Zyglo* penetrant test and found to be free of significant flaws. The microstructure of a specimen is shown in Figure 4.

*Zyglo is a trademark of Magnaflux Testing Systems Corporation for a non-destructive testing method.

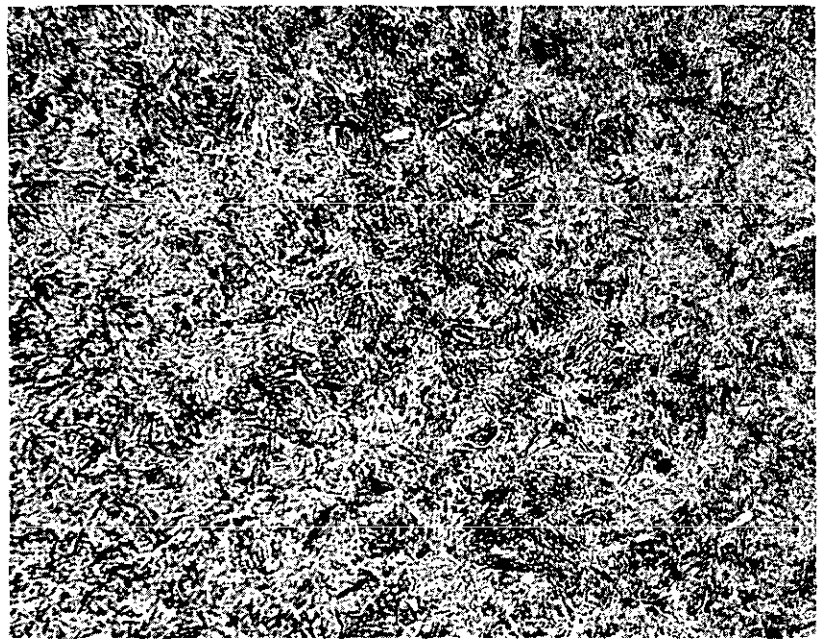

Figure 4. Microstructure of S-7 steel rods, showing Martensitic structure (400X)

The W-alloy rods were supplied by BRL. They were W-7 percent Ni-3 percent Fe alloy produced by the ERDA Y-12 plant. A description of the rods was provided by BRL and is included here as Appendix A. Mr. Silsby at BRL performed Zyglo dye penetrant tests to screen rods. Rods containing cracks were flagged as inferior quality. The rods were also examined by the Zyglo process at the University. We confirmed Mr. Silsby's observations. We also found that no rods were free from lines of pores parallel to the axis. The density of this material was found to be 17.3 g/cm^3. The hardness of these rods was Rockwell C-71.5 ± 1.

C. Launch and Sabot Techniques

When this program was begun, the intention was to do sabot development experiments and material screening with 8 g steel L/D = 10 rods. For this purpose a 20 mm diameter gun was used.

The range consisted of a 5 m long, 20 mm diameter barrel; an appropriate breech with a ballistic pressure transducer; a two-part evacuated blast tank; position detectors consisting of two channels of laser photomultipliers; four channels of 105 kV flash x-rays arranged in orthogonal pairs; two digital counters; and a sand-filled catcher tank. The principal objective of the initial test series was to demonstrate a capability to launch 8 g rods to velocities in excess of 2.45 km/s.

The first three test shots proved unsuccessful in that no x-ray photographs were obtained. During these tests, trigger of the x-ray units was accomplished by both laser/photomultiplier sensors and plywood protected Mylar foil switches. In order to avoid the pre-trigger mode in which the system seemed to be operating, the x-ray units were removed from the evacuated portion of the range. This evacuation was accomplished by eliminating the second blast tank section which had previously housed the x-ray units. The first x-ray was now directed at a region 1.5 m from the muzzle of which 0.2 m was through air at ambient pressure. Trigger of the x-rays was initiated by puncturing Mylar foil switches. These modifications did indeed enable us to obtain orthogonal x-ray photographs of the projectiles in flight. From these records projectile velocity and yaw could be calculated.

Fifteen additional test shots were fired. Rods were launched intact at velocities up to 2.3 km/s. Typical values of yaw were less than 3 degrees. These results were achieved by several redesigns of the Lexan** sabot and steel pusher plates. The most successful projectiles featured 7.6 mm thick hardened steel pushers with 13 mm thick Lexan plugs behind them. The sabots were of constant exterior diameter, and the entire launch package weighed 36 g.

In an attempt to achieve maximum velocity, the maximum charge of 110 g of 4227* propellant was employed. In that test the breech seized and the projectile broke up. It was concluded that this launch system could not successfully launch 8 g rods to the required velocity. The decision was made to terminate the subscale tests and do development testing with the 50 mm launch tube and 25 g rods.

In the first 50 mm shot, 700 g of H-870† powder was used, and the launch velocity was 2.05 km/s. It was noted that according to past experience, heavier launch packages were launched at higher velocities than lighter packages. This is an indication that the powder was not burning efficiently. A calculation of the thermodynamic efficiency of the gun seemed to confirm this. At 2 km/s and 700 g charge, the efficiency was only 16 percent. Large bore military guns, by comparison, typically achieve efficiencies of 30 percent (although at much lower velocities).

---

*A flake powder by E. I. duPont deNemours and Co. Inc.

**Lexan is a registered trademark of the General Electric Company for a polycarbonate plastic.

†A propellant produced by Hodgon Powder Company, Inc.

Improvement of powder ignition was one way in which gun efficiency could be improved. Therefore, tests RT-28 through RT-34 were tried with various design ignition tubes filled with black powder. However, little systematic improvement was obtained.

In order to improve the gun efficiency, it is necessary that the propellant develop a higher pressure before the projectile has moved significantly down the launch tube. There were three means by which this could be accomplished: use of a faster-burning powder, use of a shear disc or burst diaphram, and use of heavier launch packages. One shot with a moderate charge of 4756 powder* (RT-35) indicated that the improvement in performance from faster powder would be much less than has been observed in previous programs with small charges. Use of heavier launch packages was an unattractive idea because the extra weight must be prevented from hitting the target with the rod. However, since the forward end of the breech had a 45° taper, it was possible to add a phenolic shear disc. This resulted in a significant improvement of velocity to 2.26 km/s.

When a pressure transducer was installed in the breech, it was found that with a charge of 700 g of h-870 powder, the peak pressure was only about 140 MN/m^2 (20 ksi). Therefore, it was decided to increase the powder charge to achieve higher velocities. It was found that 1000 g of H-870 with no shear disc resulted in launch of a 217 g projectile to 2.48 km/s. Erosion to the barrel was negligible. It was clear that substantially higher launch velocities could be achieved with a shear disc or with up to 300 g more charge (the breech capacity is 1300 g). A loading curve illustrating representative data obtained during the development program and the test program is shown in Figure 5.

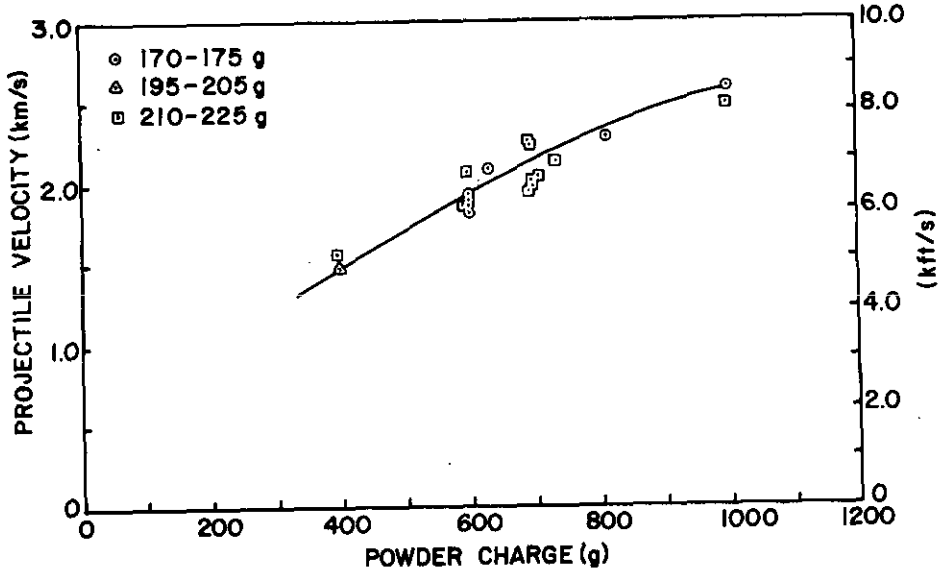

Figure 5. Loading curve of 50 mm gun for launch packages between 175 and 200 g.

*A flake powder by E. I. du Pont de Nemours & Co., Inc.

Having achieved successful launch of 25 g rods, the next problem was sabot discard. Solid sabots have a number of advantages over split sabots; they are easier to fabricate and more reproducible in performance. Therefore, a technique was devised to effect separation of a rod and a solid sabot. The essential element was a constricting tube.

The design of the constricting tube is shown in Figure 6. The tube was attached to the launch tube muzzle. The first 1.37 m of the tube was bore diameter with four slots to vent muzzle gases. The next 1.57 m was tapered. The object was to retard the sabot with respect to the rod by one rod length so that the sabot could be eliminated by means of an aperture plate. The average force required to act on the sabot was about 2.5 x 10^9 dynes (5700 lbs.). Transmission of this force to the sabot sets up maximum shear stresses in the plastic of about 35 MN/m^2 (5.7 ksi). This is also about the shear strength of polycarbonate. Since viscoelastic stresses can also be utilized, it appeared that successful operation of the constricting tube would be possible. Other difficulties were encountered which defeated the effort.

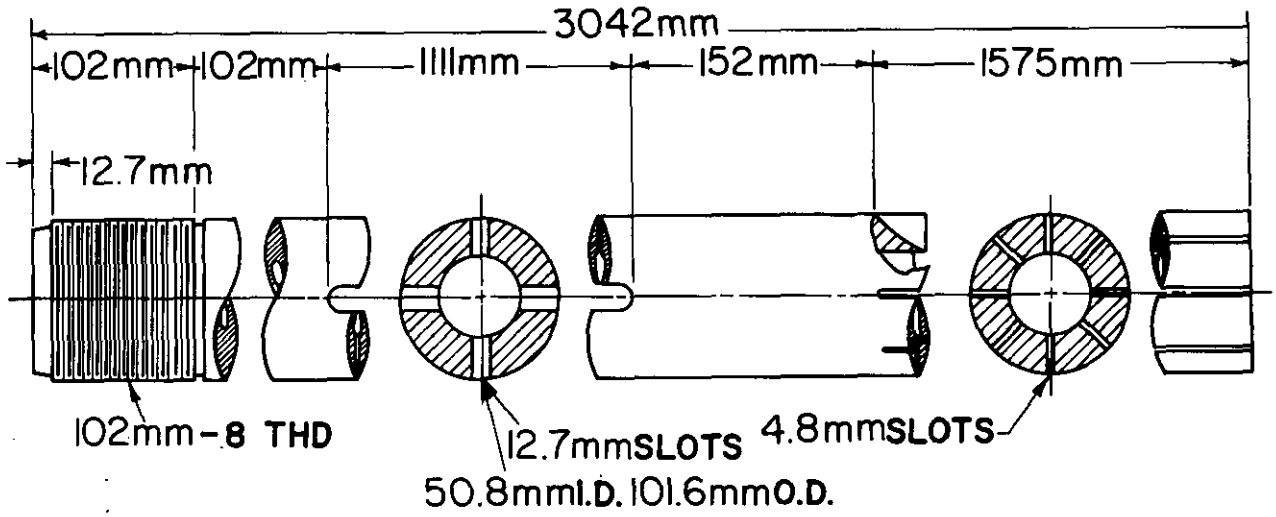

Figure 6. Design of constricting tube.

A large number of different sabot designs were tested. After some preliminary unsuccessful trials, the designs illustrated in Figure 7 through 15 developed. The first shot in this sequence was RST-100 (Figure 7). We believed that earlier sabots had failed to function properly because insufficient axial force was developed against the plastic. In this shot a copper jacket was added to increase sabot/tube friction. Silicone rubber was inserted behind the 5.6 mm pusher to reduce the forces on the rod during launch. The Lexan end cap and pusher were significantly retarded; however, the body of the

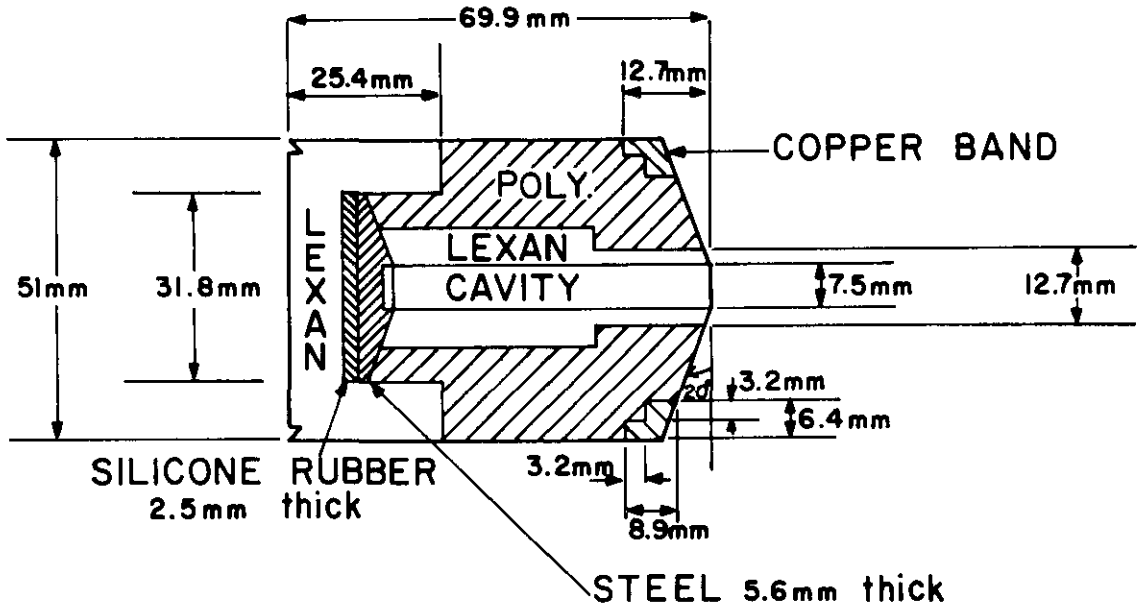

Figure 7. Sabot used in shot RST-100.

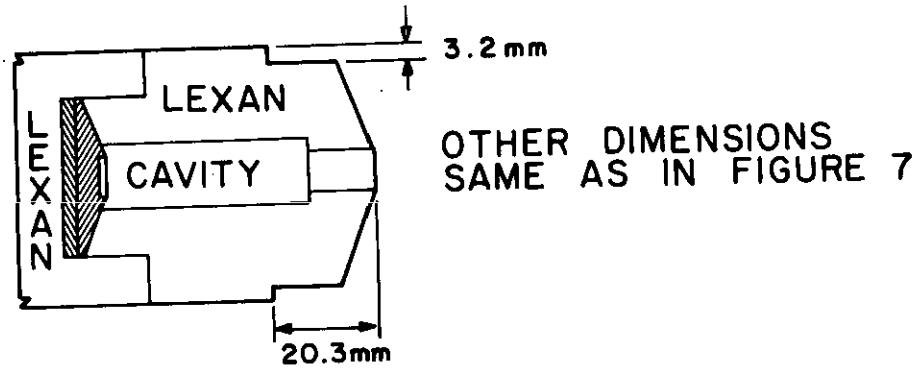

Figure 8. Sabot used in shot RST-102.

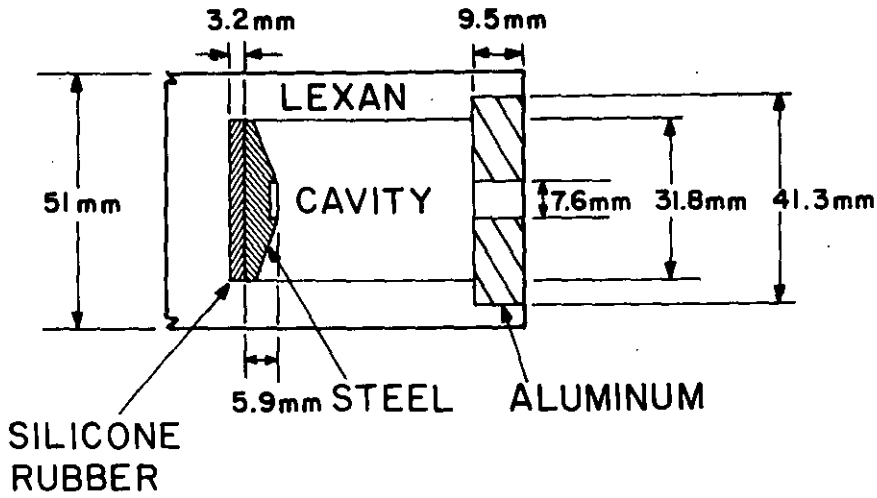

Figure 9. Sabot used in shot RST-103.

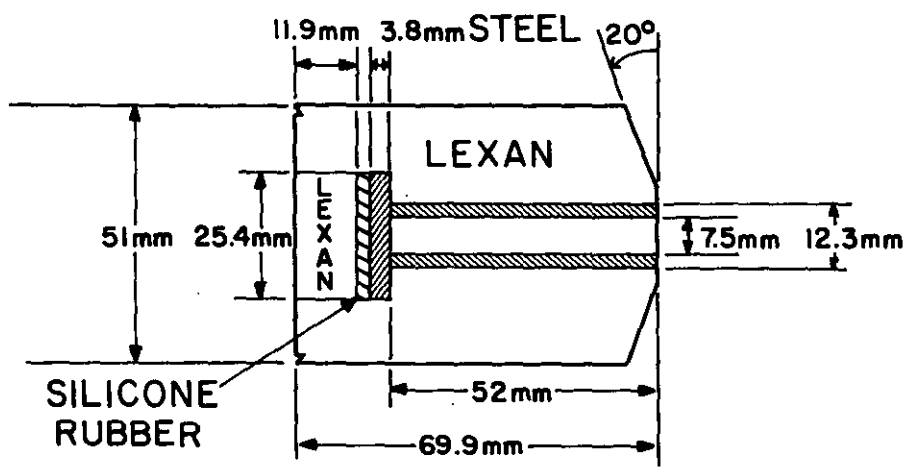

Figure 10. Sabot used in shot RST-104.

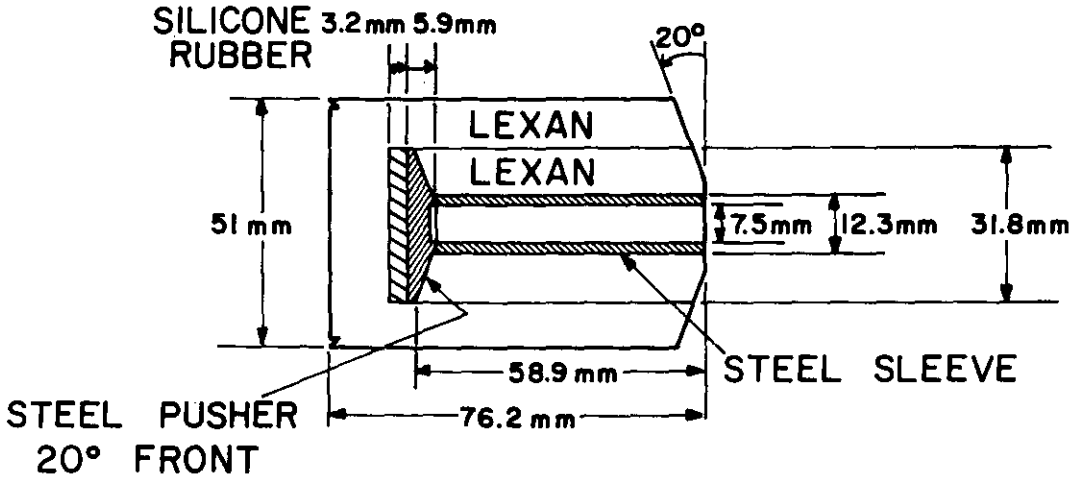

Figure 11. Sabot used in shot RST-105.

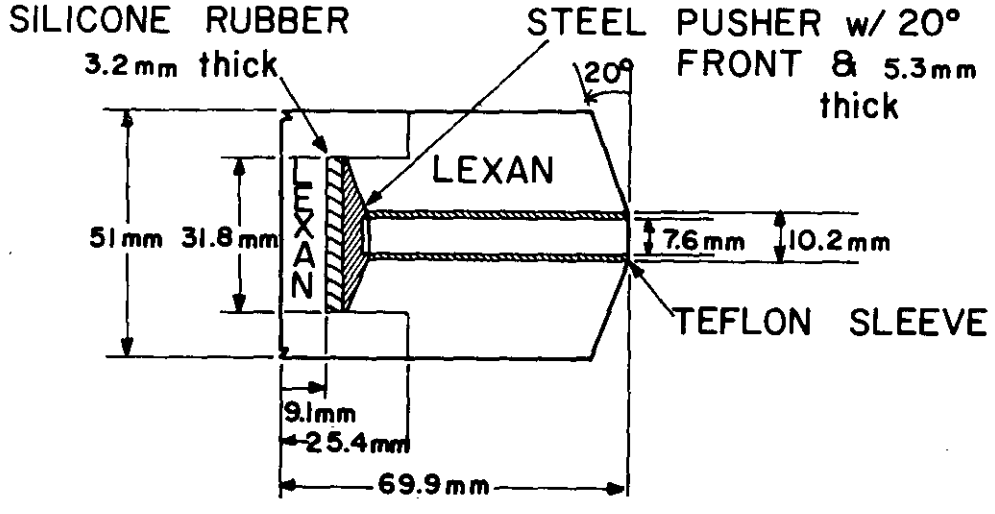

Figure 12. Sabot used in shot RST-106.

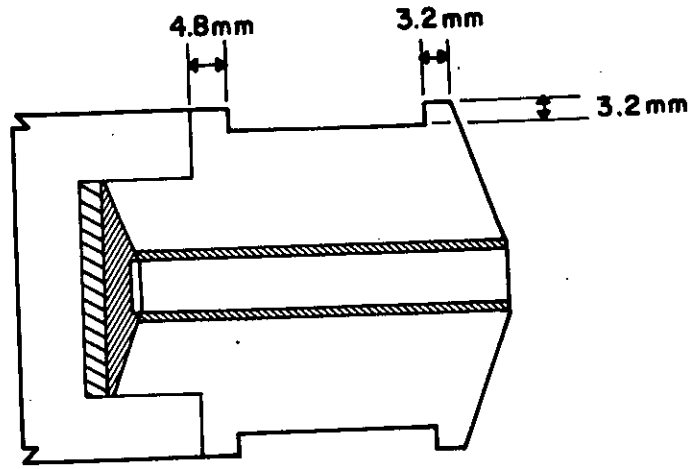

Figure 13. Sabot used in shot RST-107.

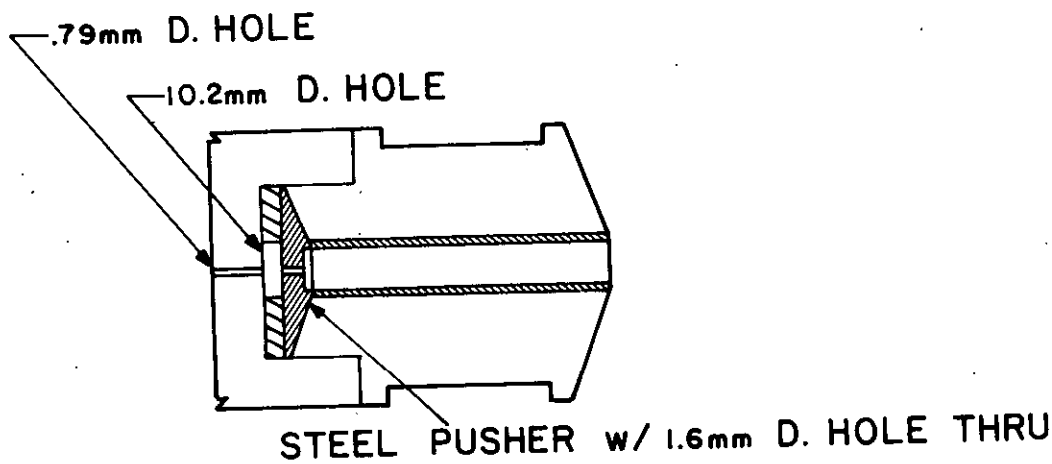

Figure 14. Sabot used in shot RST-108.

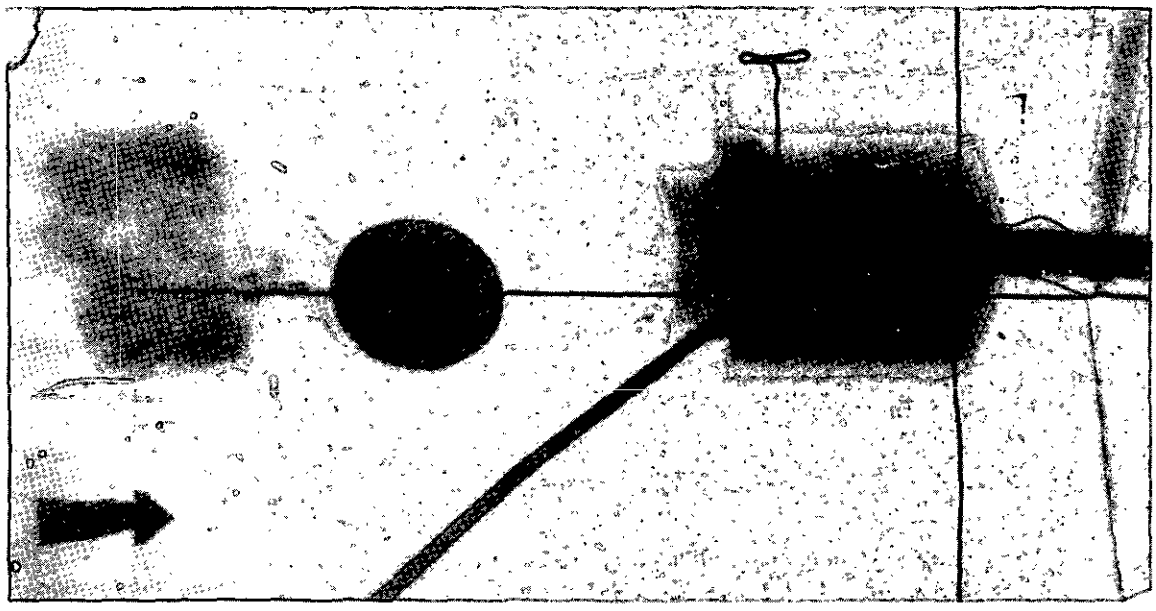

Figure 15. Radiograph of launch package in shot RST-106.

sabot emerged intact and the rod had not pulled out. The sabot was then modified to relieve the axial stress on the rod, which had apparently prevented it from leaving the sabot. Since Lexan apparently did develop adequate friction, the body of the new sabot was made entirely from that material (without the copper band) for shot RST-101. This shot resulted in a slight improvement; the rod pulled about 12 mm out of the sabot.

In order to decrease the retarding force on the rod, the design shown in Figure 8 was then tried. However, in that shot (RST-102) the sabot disintegrated. In shot RST-103 (Figure 9), an aluminum nose cap was used to support the rod lightly. In the shot, the rod pulled out of the plastic, but the aluminum ring remained attached to it. A steel tube was used in shot RST-104 (Figure 10) to reduce friction on the rod. However, the payload was apparently too heavy for the pusher, and both the rod and tube penetrated the rear end of the sabot during launch.

To prevent this from reoccurring, the front-loading sabot shown in Figure 11 was tried. During the shot (RST-105) the entire insert was apparently squeezed out of the polycarbonate collar, and, in fact, in the radiographs the Lexan insert can be seen passing over the rod and steel sleeve.

Teflon* sleeves were tried in the next three shots, RST-106, 107, and 108 (Figures 12, 13, and 14). The thickness of the

*Teflon is a registered trademark of the E. I. duPont deNemours and Co., Inc. for a series of polytetrafluoroethylene (TFE) and fluro-ethylene-propylene (FEP) plastics.

pusher plate was also reduced to 5.3 mm. The thinner pushers performed satisfactorily; however, in no case was a rod separation exceeding 12 mm observed. Figure 15 illustrates the flight of the launch package in shot RST-106.

In several of the configurations in which the rod was partially separated, the pull-out distance was increasing between the x-ray stations. It appeared that moving the stripper plate and experiment about 1 m down range would result in a functional sabot removal technique.

Moving the target area was very inconvenient, so we decided first to attempt aerodynamic sabot separation within the blast tank. We had initially been skeptical of this procedure, since the pressure in the blast tank was only 0.1 atm. The low pressure results in feeble separating forces plus a tendency for muzzle gases to yaw the package. However, we found that at 2 km/s the sabot successfully opened and the pieces could be removed from the rod with a stripper plate. Figure 16 illustrates one of the successful aerodynamic sabots which we have used. It consisted of a four-piece polyethylene shell, a 0.50 caliber two-piece glass reinforced Lexan serrated inset, a steel pusher, and a Lexan cap/obturator. Figure 17 shows this sabot opening in the target tank on shot RST-109. Successful opening before entering the target tank was achieved by slightly increasing the range pressure, and later by adding the third section to the blast tankage.

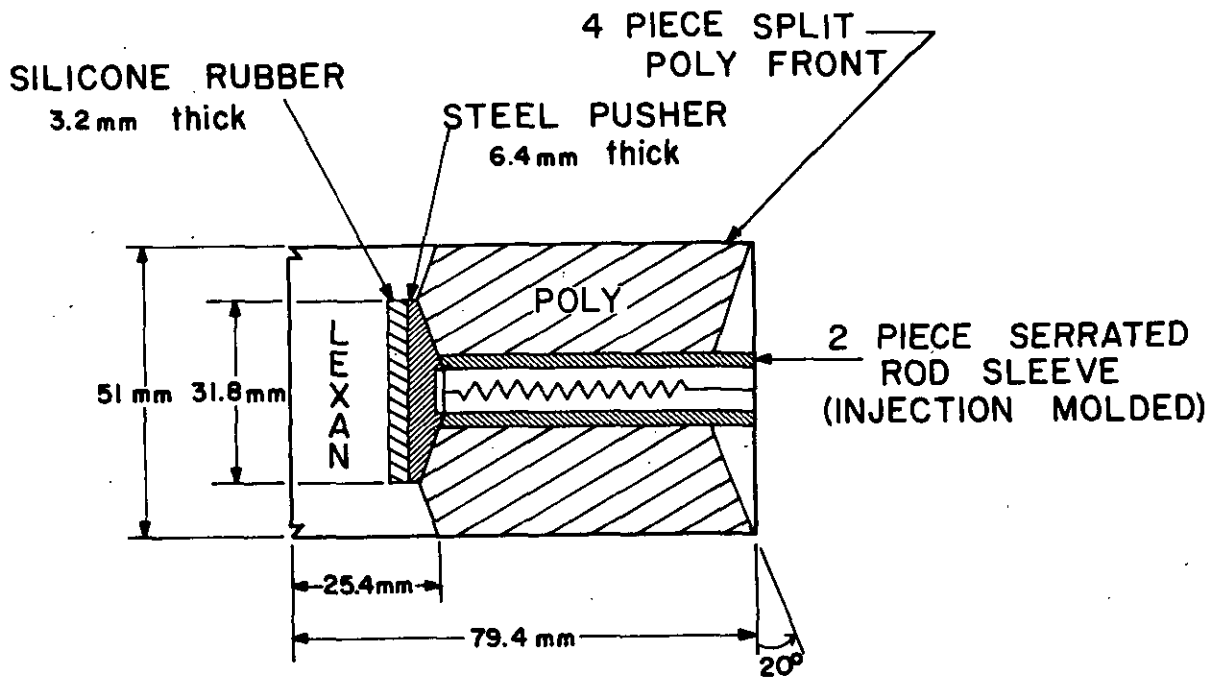

Figure 16. Aerodynamic sabot.

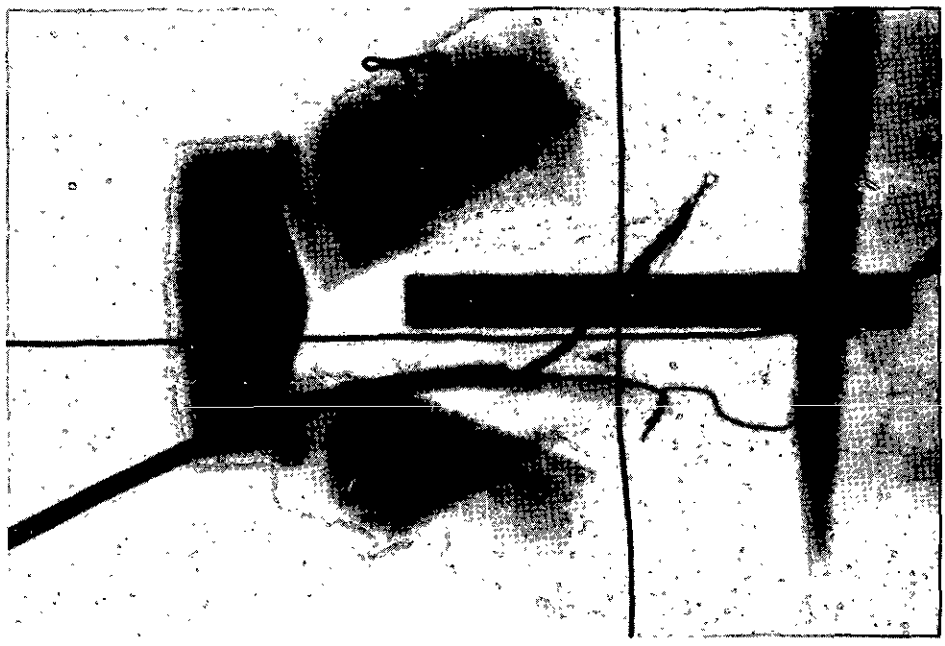

Figure 17. Aerodynamic sabot of RST-109 opening in target tank.

The split sabots were found to function with a reliability of about 65 percent at up to 2 km/s. Above that velocity the reliability fell to about 50 percent. When launch failure occurred, the rod often did not exit the blast tank. The radiographs sometimes revealed pusher plate fragments as well as rod fragments. The causes for many of the launch failures are not known. It was possible to reduce launch failures by giving attention to the following details: prelaunch yaw must be minimized; sabot collars must be low-density polyethylene, not high-density; H-870 powder, though nominally identical to military 20 mm powder, results in a slightly softer launch which is essential for launch package survival at high-charge loads; our standard foil switches, especially in a vacuum, are excessively susceptible to pretrigger from blast and small particles, and this situation can be improved by separating the two aluminum foils by a least 10 mm of styrofoam; the recess in the hardened steel pusher plate is necessary.

Two attempts were made to launch 8 g W-alloy rods with the 50 mm gun. These failed. The failures were probably related to the relatively small dimensions of the launch package. The rods were only 39 mm long, and the rest of the sabot weighed more than 150 g. The scaled free-flight distance for the small rods was also greater than for the 25 g rods. Thus, the 8 g rods were more prone to disturbance during the sabot separation process and had relatively more distance in which to tumble. Probably deflection from these sources resulted in the rods

striking the sabot stripper plate. The test experiments done with a 20 mm barrel at the beginning of the program showed that 8 g rods could be launched with that system. Thus, future shots requiring 8 g rods should be executed with a 20 mm barrel inserted deep into the blast tank.

The probable cause of launch failures was structural failure of the rod and/or pusher plate. A useful formula for calculating stress amplification in the rod projectile is

$$\bar{\sigma}_{max} = \frac{\bar{P}}{G_s} \tag{3}$$

where $\bar{P}$ is the average pressure on the base of the launch package, G_s is the ratio of the areal density of the launch package to that of the projectile (sabot factor), and $\bar{\sigma}_{max}$ is the average stress on the base of the projectile. The launch velocity, V, is given by

$$V = \sqrt{\frac{2\bar{P}\ K_T S}{K_P \rho G_S}} \tag{4}$$

where K_T is the barrel length in calibers, S is the ratio of the projectile diameter to the bore diameter, K_P is the projectile fineness ratio, and ρ is the projectile density. Hence,

$$\bar{\sigma}_{max} = \frac{K_P \rho V^2}{2SK_T} \tag{5}$$

If the pressure ratio of the gun (the ratio of peak pressure to average pressure) is Q, then

$$\sigma_{max} = \frac{QK_P \rho V^2}{2SK_T} \tag{6}$$

where σ_{max} is the highest stress experienced by the projectile. Note that σ_{max} does not depend on the sabot parameter G_S.

For the system used here, K_T = 120, ρ = 7.85 g/cm^3 (for steel) or 17.3 g/cm^3 (for W-Alloy), and G_S = 0.15 (typically). The average pressure, calculated from

$$\bar{P} = \frac{2MV^2}{\pi D^3 K_T} \tag{7}$$

where M is the launch mass (175 g nominal), D is the launch tube bore, and V = 2 km/s, is 29.7 MN/m^2 . The breech pressure transducer showed peaks of 480 to 620 MN/m^2 , which imply Q = 16 to 20. These values are probably much too high. Values of 3 to 5 are typical of high performance guns[24]. Using Q = 4 gives σ_{max} = 18 GPa (2.5 x 10^6 psi). The shear loads in the projectile and pusher are approximately given by $\sigma_{max} / \sqrt{2}$. This quantity exceeds the static shear strength of these materials by about a factor of 10. Thus, plastic deformation and possibly ultimate failure of the rod and pusher plate will occur. Indeed, several records show rods arriving short or bent, or rods accompanied by pieces of the pusher plate or both. The overstress of the projectile is proportional to Q. Thus, the success or failure of individual launches may have been very sensitive to the fraction of the peak pressure experienced by the launch package, which in turn depends on the rate of pressure rise in the breech. Examination of the pressure transducer records confirms that in shots which failed the time to peak breech pressure was usually shorter than in shots which were successful.

D. Target Description

Two types of targets were used --4340 steel and 2024-T3 aluminum. The steel was designed to be representative of armor targets and the aluminum to be representative of aircraft targets.

The steel targets were single plates of dimensions 152 mm x 152 mm x 25.4 mm. The hardness was rockwell C-30. They were gripped on the corners. The obliquity was either zero or 45°. Post-impact examination indicated that the damage was confined to the perforated region and did not extend to within several target thicknesses of the edges of the plate.

The aluminum targets were four plates, each 6.35 mm thick. They were separated by 76.2 mm (line of sight). The outside dimensions were 200 mm x 200 mm. Several shots also had 0.5 mm aluminum witness plates in front of the second, third, and fourth plates.

A scaled down version of the aluminum target was developed for the 8 g rod shots. The thickness was 4.06 mm, and the separation was 52 mm.

---

[24]AMCP 706-150, Engineering Design Handbook, Interior Ballistics of Guns.

III. EXPERIMENTAL RESULTS

Twenty-seven shots were carried out with 25 g and 8 g rods against steel and aluminum targets. Data for the configurations in Table 1 were obtained. In addition, redundant data for yawed and unyawed impacts were obtained for several configurations.

A. Summary of Terminal Effects Data

Data from the successful shots are summarized in Table 2. Table 3 provides additional behind-target data for the shots in which such data are available and are appropriate.

In Table 2, the first two columns give the shot number and matrix number. The next column gives the rod material: S-7 tool steel hardened to RC55, W-7 percent Ni-3 percent Fe alloy (Y-12 ID No. 7187-88-1477, No. 3), and WC (13 percent Co). The mass of the rods was 25 g. The L/D ratio was ten, and the noses were hemispherical. The launch velocities were either measured from radiographs or estimated from the gun-loading curve. The estimated velocities are ± 0.03 km/s.

For all the shots for which pre-impact radiographs were obtained, the yaw angle and direction are given in the table. The directions are referred to standard spherical polar coordinates with trajectory along the +X direction and the +Z axis vertically up; this coordinate system is diagrammed in Figure 18. The steel targets were 4340 plates, 25.4 mm thick, approximately 150 mm x 150 mm face dimensions, and hardened to RC30. The inclined targets were rotated about the Z axis, so that a normal to the rear surface lies in the horizontal plane at $\theta = 45°$. The aluminum targets were spaced arrays, as described in the table.

The terminal effects parameters given in the table include principal fragment velocity and mass. The masses of the principal fragments were measured by weighing the recovered fragments or from the aspect ratios of the images on the radiographs. Also included is a column for the total area lost from the half-millimeter witness plates placed behind the target. The next column reports the number of perforations in the particle board placed behind the target. The last column of the table contains remarks.

Additional behind-target data are presented in Table 3. These data were derived from the behind-target radiographs. The fragments reported in these tables are ones which perforated the particle board placed behind the witness plate. The screening effects of this particle board are extensively discussed later in this report. The table gives the mass, velocity, and direction of each fragment.

TABLE 1. SHOT MATRIX

EXPERIMENTAL CONFIGURATION	ROD MASS (g)	ROD MATERIAL (g)	TARGET DESCRIPTION	IMPACT VELOCITY (km/s)	OBLIQUITY (deg)
R1	25	S-7	25 mm 4340 R_C 30	2.0	0
R2	25	WC	25 mm 4340 R_C 30	2.0	0
R3	25	W-Ni-Fe	25 mm 4340 R_C 30	2.0	0
R4	25	S-7	25 mm 4340 R_C 30	2.0	0
R5	25	WC	25 mm 4340 R_C 30	2.0	45
R6	25	W-Ni-Fe	25 mm 4340 R_C 30	2.0	45
R7	25	WC	4 Al plates, 2024-T3 6 mm thick, 50 mm apart	2.0	0
R8	25	W-Ni-Fe	4 Al plates, 2024-T3 6 mm thick, 50 mm apart	2.0	0
R9	25	S-7	25 mm 4340 R_C 30	2.5	0

TABLE 2. SUMMARY OF BEHIND-TARGET DATA

IDENTIFICATION		PROJECTILE PARAMETERS				TARGET PARAMETERS		TERMINAL EFFECTS				
Shot No.	Config-uration	Rod Mat'l[1]	Launch Velocity (km/s)	Yaw	Remarks	Target[1]	Obliq[2] (deg)	Vel.of Prin. Frag. (km/s)	Mass of Prin. Frag.	Lost Area from Witness Plate (mm^2)	# of Perfs. of Particle Board	Remarks
111	-----	S-7	1.87[3]	NA	sm. bend	mild steel	0	1.70	15.6	-----	NA	
112*	R1	S-7	1.87[3]	~0	~6° bend	steel	0	0.42	6.5[4]	736	17	
113	R1	S-7	1.87[3]	~1°	--------	steel	0	1.65	15[4]	690	1	
114	R3	W	1.87[3]	~3°	--------	steel	0	NA	16[4]	1104	18	rod fragment >38° bend at ~20° departure angle-fragments included 2.35 g steel chunk
115	R2	WC	1.87[3]	NM	--------	steel	0	1.65	-----	2711	9	debris cloud,centered at 12°departure angle
116*	R3	W	1.87[3]	~1°	~1° bend	steel	0	1.69	17[4]	950	10	rod fragment ~12° bend
117	R6	W	1.81	8°	-------	steel	45	NA	NA	599	13	no significant central fragments; two principal fragments at ϕ=68° θ=20°; 4.3g rod fragment part or all of principal fragment pkg.
118*	R6	W	1.86	12° θ=5.5,ϕ=79		steel	45	1.52	8.5	890	6	
119	R5	WC	1.87[3]	11° θ=10,ϕ=85		steel	45	1.50	-----	1033	3	cloud
120	R4	S-7	1.90	14° θ=-10,ϕ=80		steel	45	NA	NA	140[5]	2	
121*	R4	S-7	1.91	NA		steel	45	1.20	9.2	176[5]	4	
124	R8	W	1.87[6]	~16° θ=10,ϕ=77		Al	0	1.76[6] 1.71	-----	426	4	rod fragment direction θ=.04,ϕ=122 yaw data; 16.2° through 1st plate; 13.8° at last plate 5.8° behind last plate
125*	R8	W	2.12	36°[7] θ=-22,ϕ=61		Al	0	1.40	21.2	1046	11	rod bent 90° at exit
130	R7	WC	1.84[6]	23°	2nd half of rod broke up on launch	Al	0	1.37	-----	855	8	debris cloud was undeflected
131	test	S-7	2.58	~0	--------	----	----	-----	----	----	----	
135	R9	S-7	2.27 ±.07[3]	NA	--------	steel	0	2.10	15	1706	5	no intermediate size fragments initial behind target yaw 10° center hole 60 mm dia.

*additional fragment data available in Table 3
[1]steel targets are 25.4 mm thick 4340, RC30. Aluminum targets for 25g rods are 4 pcs, 6.35 mm thick separated by 76.2 mm.
[2]target plane is rotated about Z axis (θ=45°)
[3]approximated from gun loading curve.
[4]estimated from image size.
[5]a significant number of fragments missed the witness plate
[6]average velocity between first and fourth plate.
[7]yaw was 43° halfway through first plate.

TABLE 3. BEHIND TARGET FRAGMENTS WHICH PERFORATED PARTICLE BOARD

SHOT NUMBER	MASS (g)	VELOCITY (km/s)	DIRECTION θ	DIRECTION φ	REMARKS
112	6.5*	0.42	30	99	
	1.6*	0.38	43	104	
	1.6*	----	--	---	High angle
	0.336	0.32	--	---	High angle
	0.225	0.35	9.1	88	
	-----	0.64	9.4	80	
	-----	0.28	7.8	88	
	-----	0.34	-1.2	79	
	0.042	0.04	15	97	
	0.047	0.35	15	91	
	-----	0.33	1.0	95	
116	17.0*	1.69	1.7	97	Rod fragment
	0.144	1.35	-0.7	95	Rod fragment
	0.078	1.60	-1.4	96	Rod fragment
	0.075	1.74	8.1	93	Rod fragment
	0.068	1.34	9.3	100	Rod fragment
	0.138	1.60	0.7	99	Rod fragment
	0.081	1.80	-0.6	100	Rod fragment
	0.169	1.60	-1.1	101	Rod fragment
	0.052	1.46	-0.7	86	Rod fragment
	-----	1.74	12.9	103	Rod fragment
118	8.5	1.52	-2.8	105	Rod fragment
	---	----	-4.2	100	
	---	1.46	-8.7	96	
	---	1.75	-9.7	97	
	0.086	1.25	-10.8	98	Rod fragment
	0.144	1.28	-11.7	97	
121	9.22	1.30	-24.9	92	Rod fragment
	0.212	1.30	-27.3	81	Target fragment
	-----	----	-26.9	105	
125	21.2*	1.35	-8.6	80	Rod fragment
	2.97	1.02	1.0	83.5	Rod fragment†
	2.102	1.08	-7.0	86	Rod fragment
	0.167	1.00	-3.8	83	Rod fragment
	0.259	0.95	9.4	90	
	0.896	----	-2.2	91.2	Pusher plate frag.
	0.015	0.73	0.0	94	
	0.484	0.63	0.0	87	Rod fragment
	0.630	0.73	3.6	99	Target fragment
	0.095	0.59	11.3	94	Target fragment
	0.225	----	----	--	Rod fragment

* estimated from size of image on radiographs
† recovered as two particles

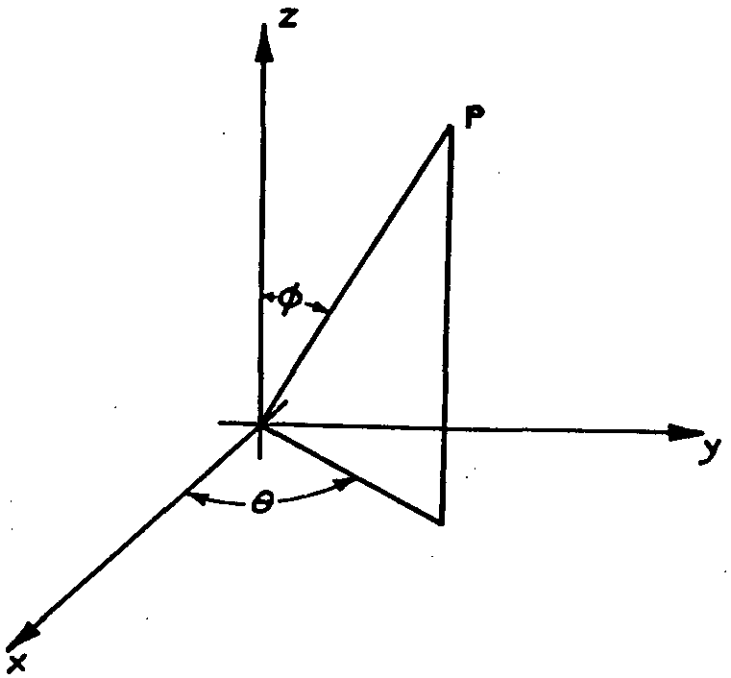

Figure 18. Coordinates. Trajectory is along x-axis (θ=0,ϕ=90°).

B. Discussion of Radiographs

In this section, we present and discuss most of the radiographs. The radiographs here printed present the perspective which a viewer would have of the events in the target chamber if he were looking from the position of the x-ray sources. In terms of coordinates, this is roughly at ϕ = 0, ϕ = 90°, and θ = 90°. The radiographs here are not all printed to the same magnification.

The first shot against a steel plate was performed in order to test the behind-target data collection techniques. It was designated RS-111. A standard S-7 tool steel rod was launched at 1.87 km/s against a 25.4 mm thick mild steel plate hardened to Rockwell "B" 85. A 0.5 mm aluminum witness plate was placed 369 mm behind the target plate. No particle board was placed behind the witness plate.

The rod bent slightly on launch. One of the behind-target radiographs is shown in Figure 19. The residual velocity was determined to be 1.7 km/s by placing a threaded rod in the target chamber along the path followed by the fragment and counting the number of threads between the position of the fragment in the radiographs. The rod emerged at an angle of about 30° to the original trajectory. Its length appeared to be reduced by about 25 percent, it was tumbling, and it had a single large bend. Clearly it would not have been very effective against a second plate, although it did perforate 160 mm

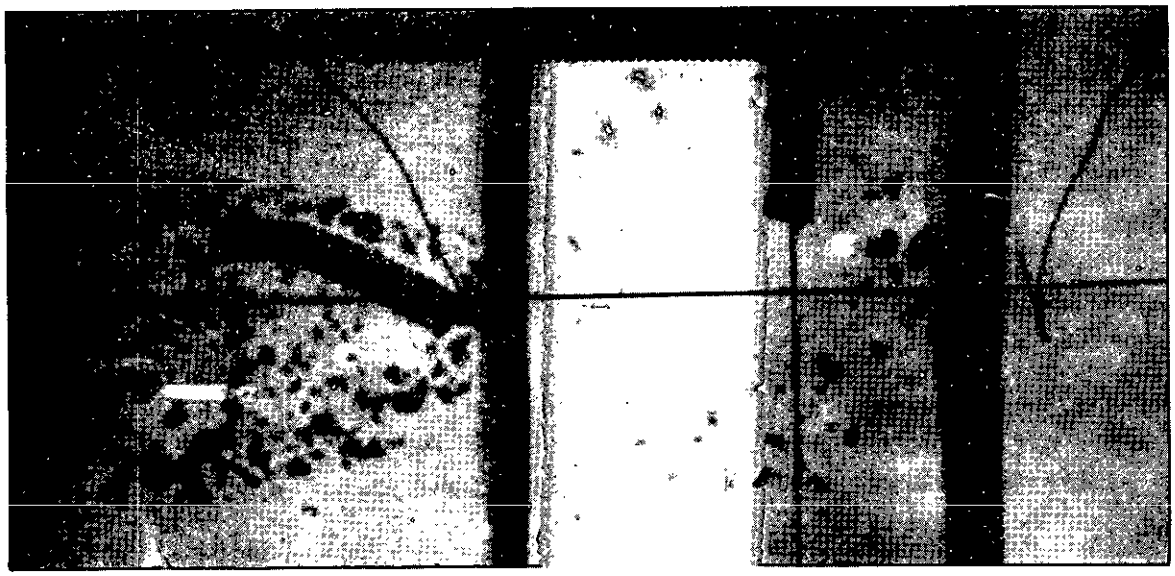

Figure 19. Behind-target radiographs of S-7 rod in shot RS-111 (In this and subsequent radiographs, the rod moves left to right).

of wood in the catcher array. The mass of the recovered rod fragment was 15.6 g.

There were a large number of perforations in the witness plate. It is also clear from the radiographs that most of the particles in the debris cloud were very slow. It was not practical to collect such a large number of particles from the catcher blocks; hence, the particle board was added.

The data shots commenced with shot RS-112. The target was Rockwell "C" 30, 25.4 mm thick 4340 steel plate; and the rod was S-7 tool steel. In RS-112, the rod was bent about 6° on launch. The rod broke up as it penetrated the steel plate, and the residual velocity was so small that it appears that the impact velocity was near the ballistic limit. Figure 20 shows one of the behind-target radiographs. The task of fragment counting was made easier by placing 19 mm of 0.70 g/cm^3 particle board behind the witness plate. This aided discrimination between high-energy metal fragments and other less lethal particles projected behind the target. There were now only 17 fragments which entered the block array.

Shot 113 was a repeat of matrix element R1 in which the rod did not bend. In order to reduce further the number of fragments entering the wood blocks, two sheets of particle board were placed behind the witness plate. Figure 21 shows one of the behind-target radiographs from that shot. The rod was

Figure 20. Behind-target radiograph of S-7 rod in shot RS-112.

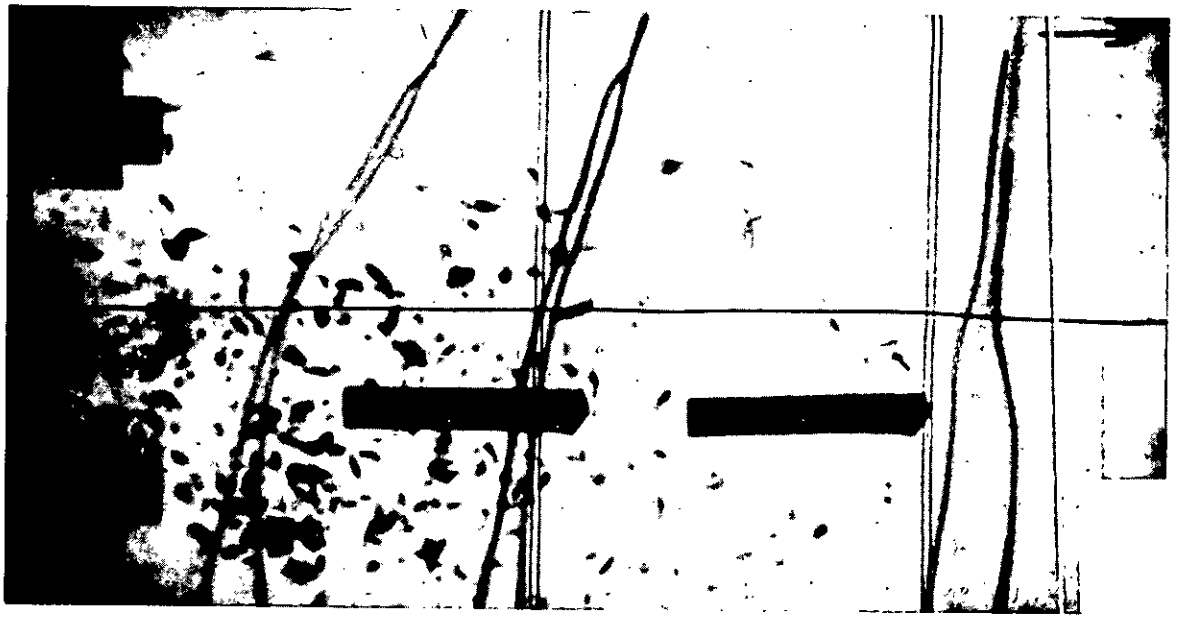

Figure 21. Behind-target radiograph of S-7 rod in shot RS-113.

about 40 percent consumed, but the remaining portion emerged intact at a velocity of 1.65 km/s. The tip of the rod fragment appeared sheared off at approximately 45° to its axis. There was only one substantial perforation in the witness plate and only two perforations of the first 38.1 mm thick particle board, the central one and one at a high angle (approximately 30°). Comparison of this shot with RS-112 indicates that slight deviations from straightness greatly reduce penetration capability.

Shot RS-115 was for the same configuration with a WC rod (matrix element R2). This rod disintegrated on impact, as shown in Figure 22. The velocity of the front of the debris cloud was 1.65 km/s, the same as in shot RS-113. The direction of the cloud front was approximately $\theta = -5.2°$, $\phi = 78.7°$. There were nine separate perforations of the 38.1 mm thick particle board. Unfortunately, due to the opaqueness of the debris, individual velocities could not be assigned to these perforations.

Figure 22. Behind-target radiograph of WC rod in shot RS-115.

Shot RS-116 was for the same configuration with a 25 g W-Ni-Fe rod (matrix element R3). This was a repeat of shot RS-114, for which incomplete behind-target radiographs were obtained, due to x-ray malfunction. In RS-116 and subsequent shots, 38.1 mm of 0.75 g/cm^3 particle board backing was placed behind the witness plate. Two sheets of equal thickness were employed. The two orthogonal radiographs taken immediately prior to impact are shown in Figure 23. (The first set of radiographs were lost due to screen pre-triggers.) They show that the rod was slightly bent on launch (in the direction $\phi \sim 90°$, $\theta \sim -1°$). The nose of the rod appears abnormal in the

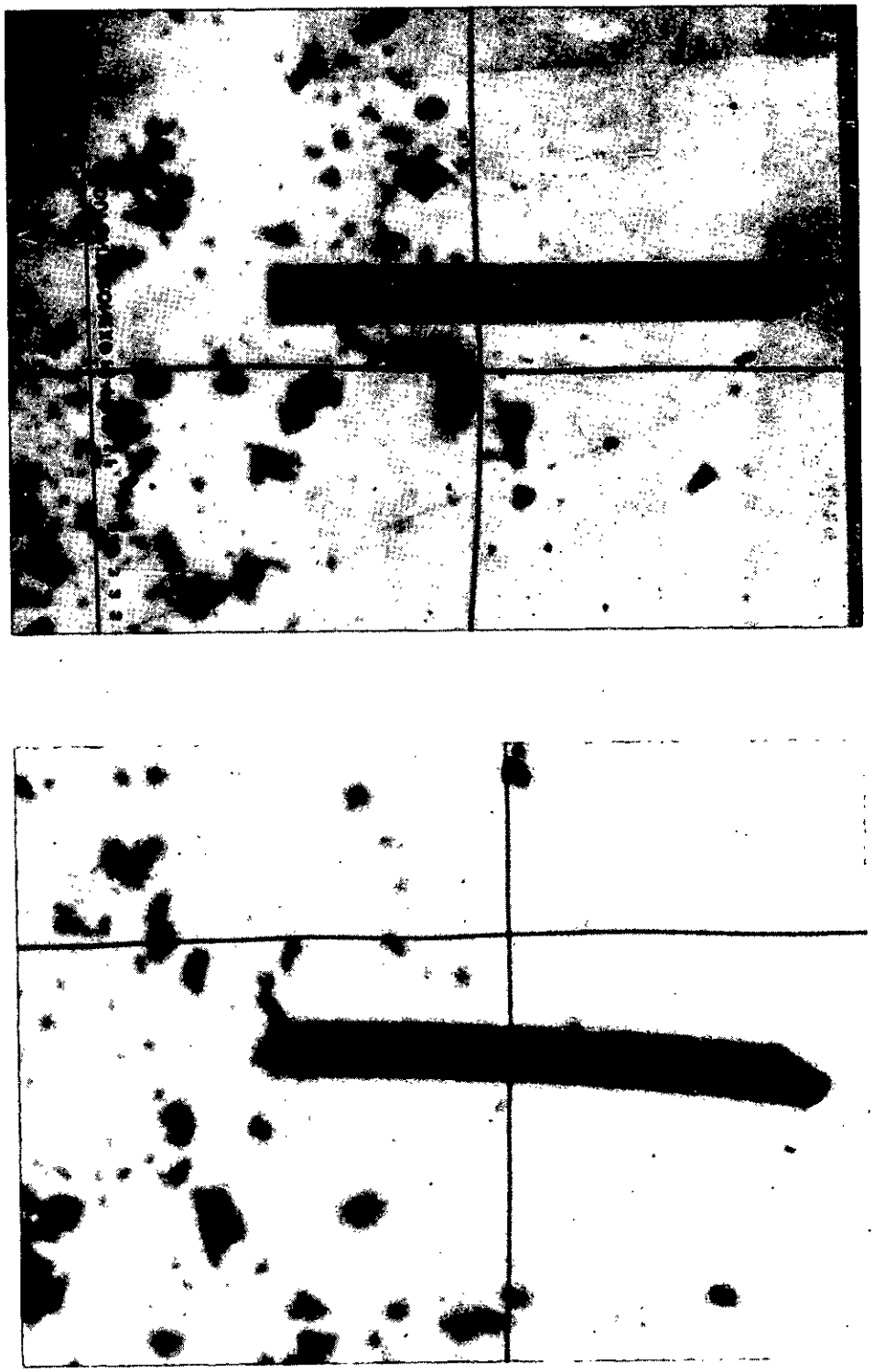

Figure 23. Two orthogonal view of pre-impact W-Alloy rod in shot RS-116.

in the bottom radiograph. The aspect ratio of the rod in the radiograph is about 6 percent too large, so apparently some material from one of the velocity screens is stuck on the nose. One of the behind-target radiographs is shown in Figure 24. The single large fragment is apparently the tail end of the rod; it is bent about 12°, is rapidly tumbling, and is traveling at 1.69 km/s. The fragment identifications listed in Table 3 were accomplished by density measurements.

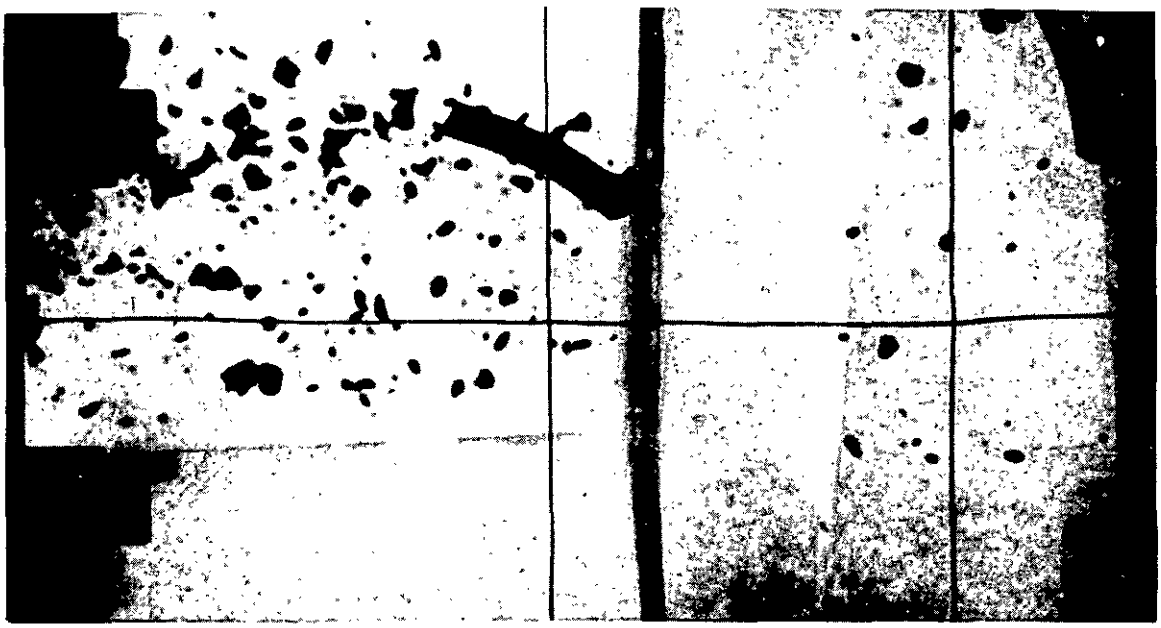

Figure 24. Behind-target radiograph of W-Alloy rod in shot RS-116.

The shots against 45° obliquity targets commenced with RS-117 for which good behind-target data was not obtained. The matrix element R6 was repeated in RS-118. Unfortunately, the rod struck with 18° yaw (away from the target, as shown in Figure 25). The behind-target radiographs showed two major fragments, as illustrated in Figure 25 and tabulated in the data tables. We note that the fragment patterns for RS-117 and 118 seemed to differ marketly; in RS-117 the fragments were small and at high departure angles, while in RS-118 they were central. In RS-117 the pusher plate had broken up. The radiographs show an intact, slightly yawed rod surrounded by pieces of the pusher plate. These may have struck the rod during penetration and led to breakup and deflection of the fragments.

Shot 119 was a WC rod against the inclined target. As expected, the radiographs showed that the rod disintegrated during perforation.

Shot 121 was a successful execution of matrix element R4, an S-7 rod against the 45° obliquity target. Only one pre-impact picture was obtained. It is shown in Figure 26. In

Figure 25. Behind-target radiograph of S-7 rod in shot RS-118 (Oblique target).

Figure 26. Pre-impact radiograph of S-7 rod in shot RS-121.

that plane, yaw was negligible and there was a very slight bend. Views of the one principal fragment, which emerged at a small deflection angle, are shown in Figure 27.

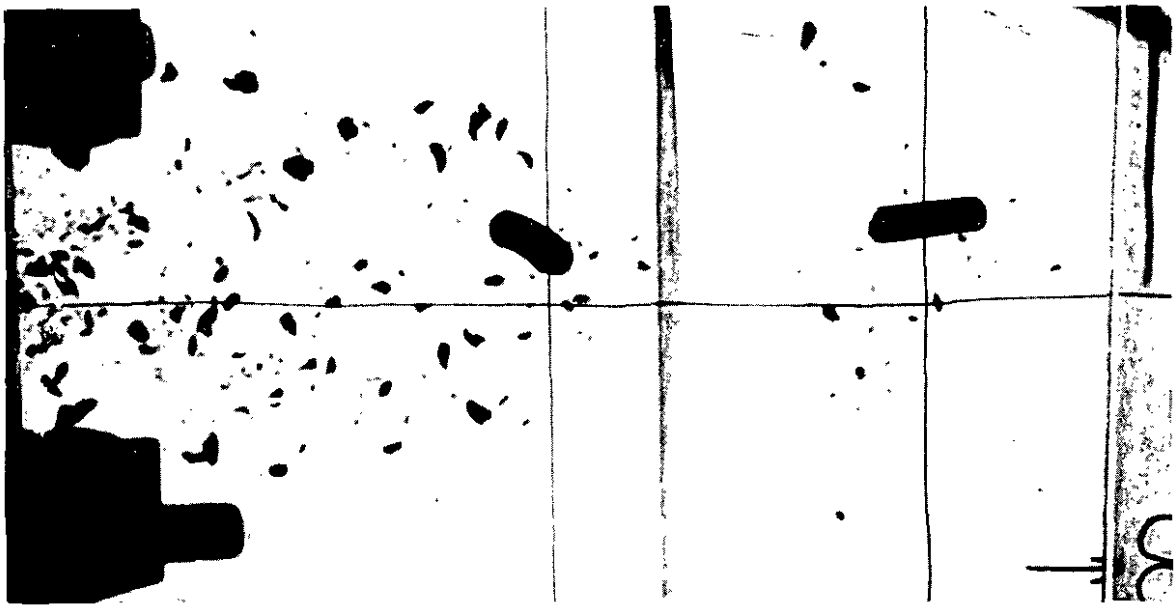

Figure 27. Behind-target radiograph of S-7 rod in shot RS-121.

Aluminum targets were impacted with W-Alloy and WC rods. The target consisted of four plates of 6.35 mm thick aluminum spaced 76.2 mm apart. Witness plates 0.5 mm thick were placed in front of the second, third, and fourth plates.

The W-Alloy rods were very effective at penetrating aluminum. Even though the rods hit yawed in Shots 124 and 125, they did not fragment or significantly deviate from their initial direction. In Shot 124, the initial yaw angle was approximately 16°; and the yaw decreased during penetration. This is shown in Figure 28. In Shot 125, the initial yaw was 36°; and the yaw increased during penetration, as shown in Figure 29.

In Shot 130, a WC rod disintegrated as it penetrated the target. This process started at the nose after the first plate perforation. A sequence of radiographs showing the WC rod penetrating a spaced-aluminum target is shown in Figure 30. It can be seen that by the time the third plate was perforated, the rod had completely fragmented.

Several test shots were performed at this point in the program to perfect high-velocity launch techniques. In Shot 131 we succeeded in launching a S-7 rod to 2.58 km/s with insignificant yaw or bend. However, the success could not be repeated; and it was finally decided to conduct an experiment

Figure 28. Radiographs showing W-Alloy rod during penetration of spaced aluminum target in shot RS-124. First image shows rod as it penetrates first plate, second image shows rod as it strikes last plate.

Figure 29. Radiograph showing W-Alloy rod during penetration of spaced aluminum target in shot RS-125. Exposures are at last plate and behind-target.

Figure 30. Radiograph showing penetration of WC rod through spaced aluminum target. (Exposures are between first and second plates, as fourth plate is struck, and behind the target.)

at a velocity less than the matrix value (Table 1, R9) of 2.5 km/s.

Shot 135 was relatively high-velocity impact (2.27 km/s) of a S-7 rod against a 0° obliquity 25.4 mm thick RHA plate. A sample behind-target radiograph is shown in Figure 31.

The damage to the rod does not appear to differ from those sustained in lower velocity impacts. The witness plate also indicated an absence of high-angle fragments. The increased energy in the fragments, however, was very evident in the damage done to the catcher array.

C. Fragment Directions

The directions of the principal fragments were studied in order to detect correlations with yaw direction or target obliquity. The fragment directions are expressed in terms of departure angle θ_D and angle of orientation ϕ_o as defined in Reference 25. These angles are related to the spherical coordinates (ϕ,θ) by the following equations:

---

[25]Grabarek, C., L. Herr, "X-Ray Multi-Flash System for Measurement of Projectile Performance at the Target," BRL TN 1634, September 1966. (AD #807619)

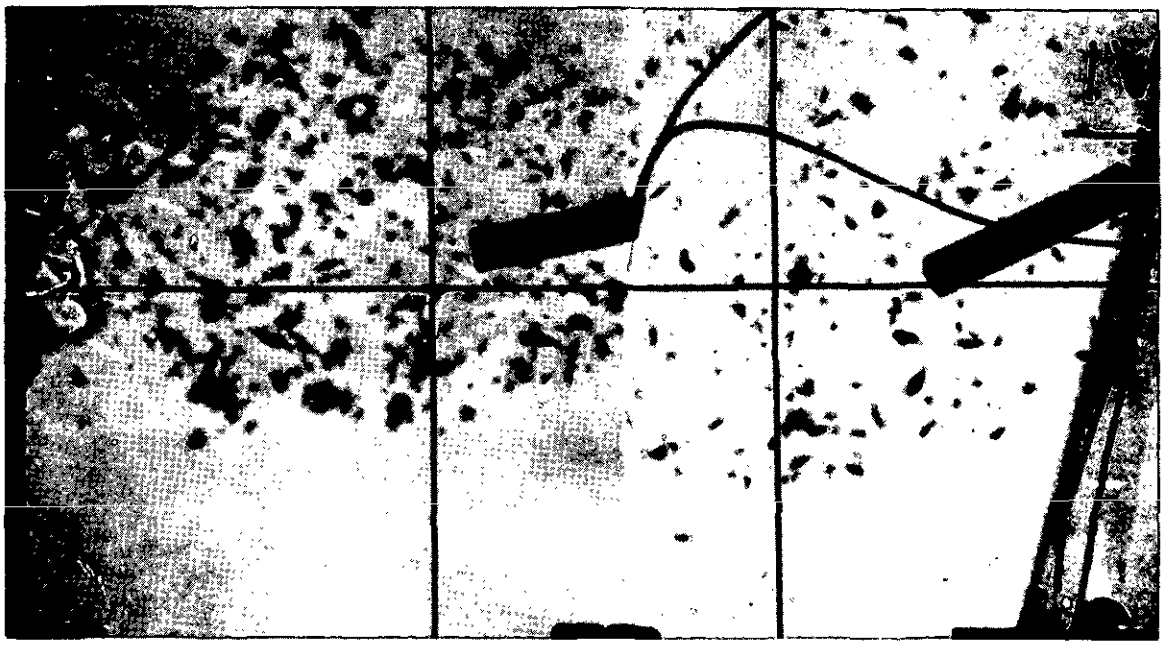

Figure 31. Behind-target radiograph of S-7 rod in shot RS-135.

$$\cos \theta_D = \sin \phi \cos \theta$$
$$\tan \phi_o = \sin \theta \tan \phi \qquad (8)$$

Figures 32 through 39 depict the departure and orientation angles for yaw, principal fragment direction, and target obliquity for the shots for which all of these quantities are known. The following observations can be made:

- In three out of four cases of tough penetrators (S-7 and W-Alloy) versus monolithic targets, the principal fragment and yaw directions were anticorrelated.
- For W-Alloy rods striking multilayer aluminum targets, the principal fragment and yaw directions were positively correlated.
- There is no discernible relationship between the target obliquity and the magnitude or direction of the principal fragment deflection.

The data from Shot 112 are the most difficult to interpret. The rod in this case was slightly bent prior to impact. Its residual velocity was anomalously low, and the departure angle was anomalously high. Figure 40 shows one of the pre-impact radiographs for that shot. Two conclusions seem possible: Fragment direction is extremely sensitive to pre-impact rod deformation or the rod was really fractured and/or the portion

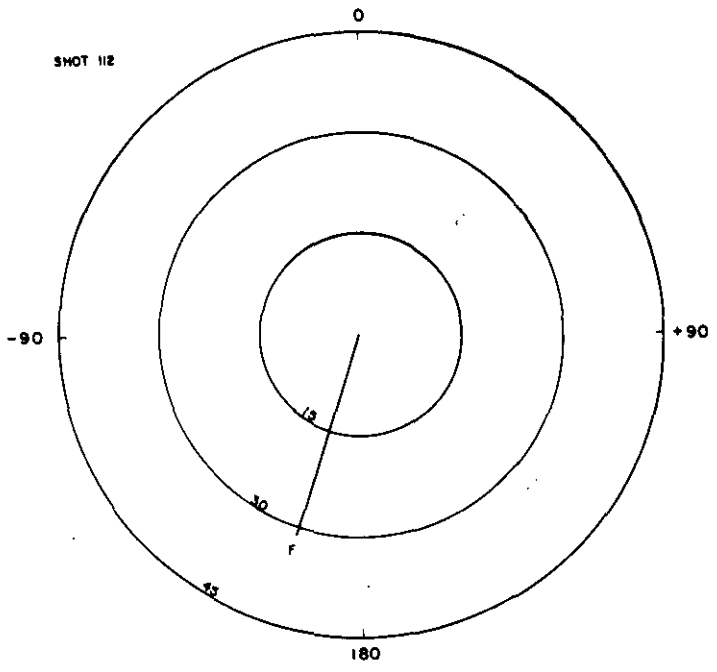

Figure 32. Principal fragment directions from shot 112. Direction of Line F indicates orientation angle. Length indicates departure angle (S-7 rod). Note that this rod was slightly bent prior to impact.

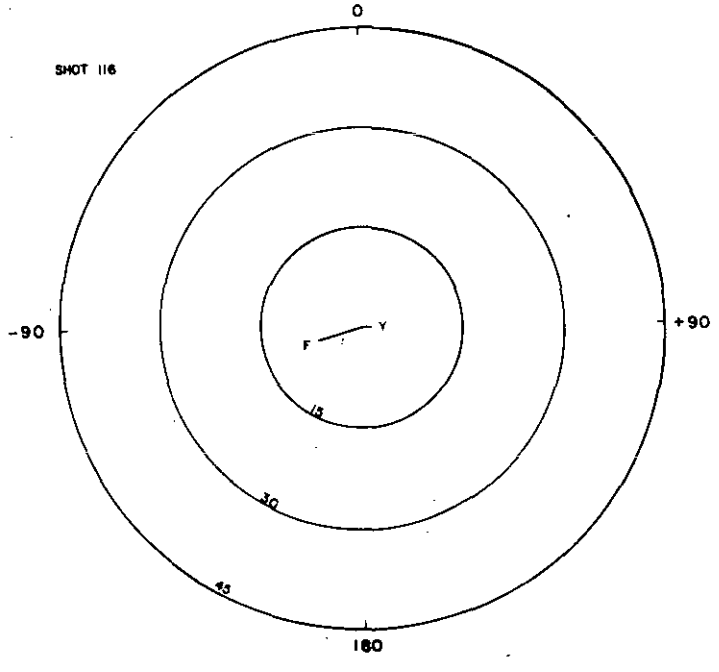

Figure 33. Incoming yaw direction (Y) and principal fragment direction (F) for shot 116. (W-Alloy rod).

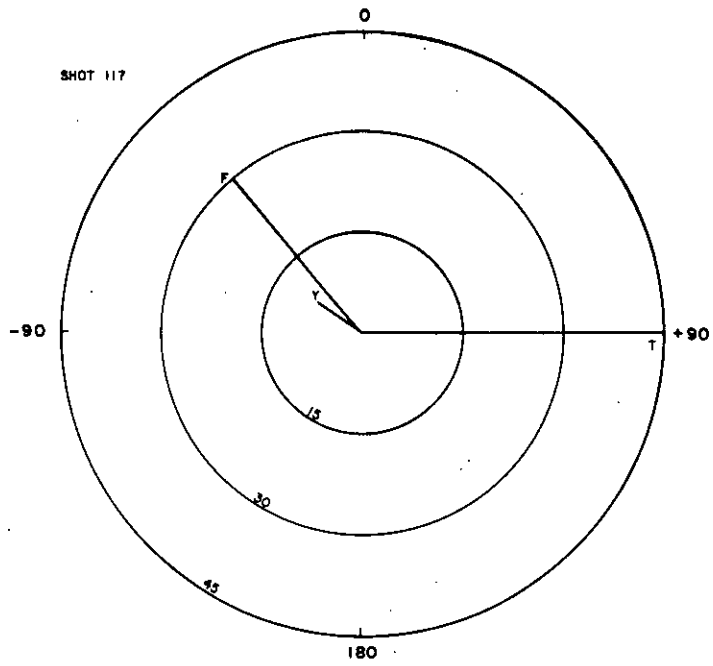

Figure 34. Incoming yaw (Y), principal fragment direction (F), and target orientation (T) for shot 117 (W-Alloy rod).

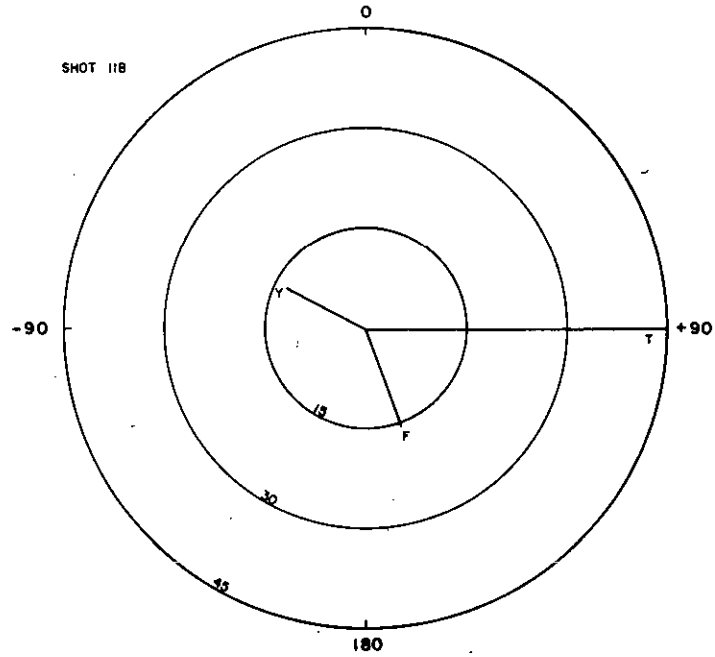

Figure 35. Incoming Yaw (Y), principal fragment direction (F) and target orientation (T) for shot 118 (W-Alloy rod).

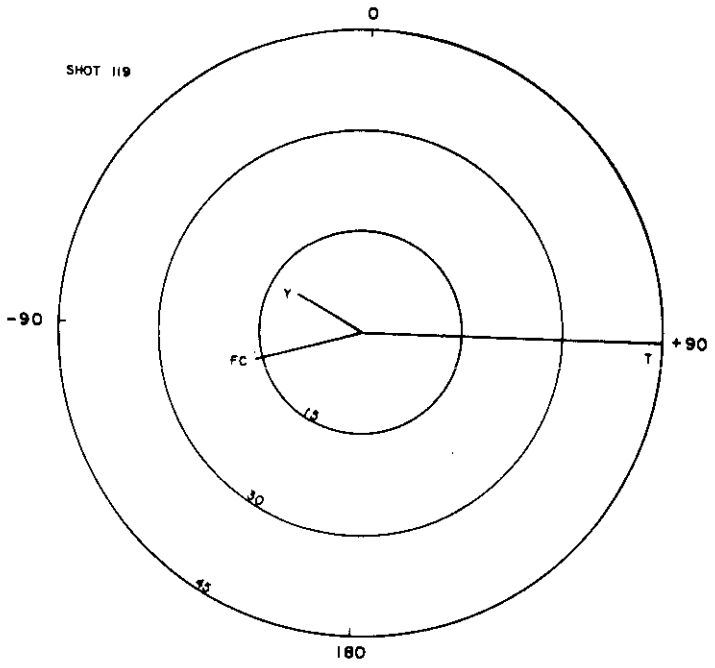

Figure 36. Incoming yaw (Y), direction of fragment cloud (FC), and target orientation (T) for shot 119 (WC rod).

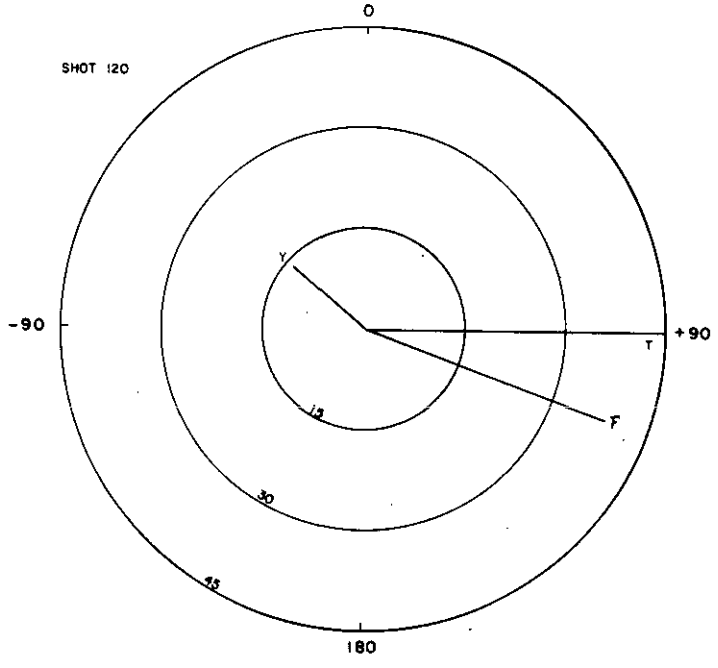

Figure 37. Incoming yaw (Y), principal fragment direction (F), and target orientation (T) for shot 120 (S-7 rod).

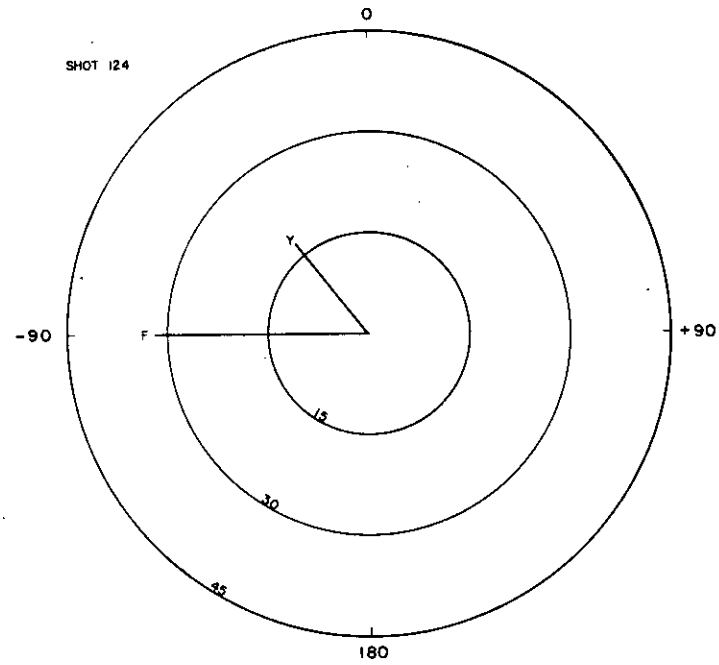

Figure 38. Incoming yaw (Y), principal fragment direction (F), for shot 124 (W-Alloy rod, aluminum target).

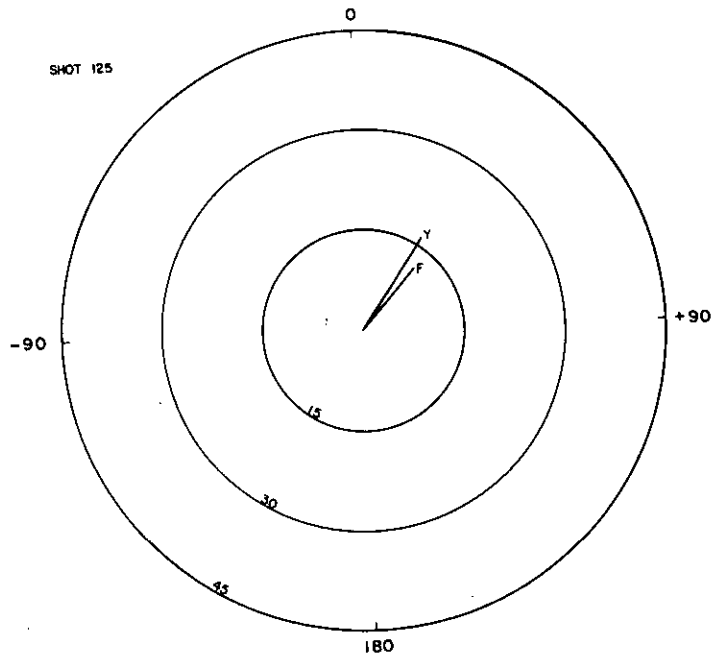

Figure 39. Incoming yaw (Y), principal fragment direction (F), for shot 125 (W-Alloy rod, aluminum target).

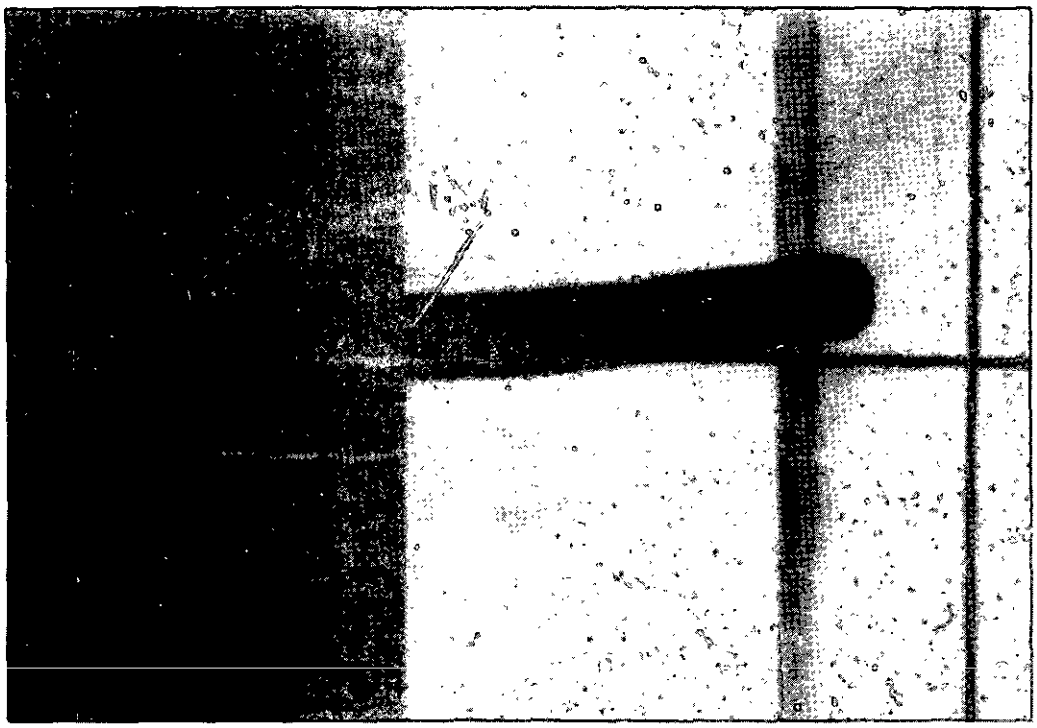

Figure 40. Pre-impact radiograph from shot RS-112.

observed in the photograph was broken off and at least part of it hit the target very highly yawed. We suscribe to the second hypothesis because of the extremely low residual velocity of that shot.

The lack of good correlation between yaw or target obliquity and fragment direction is surprising. Possibly an interrelationship exists between these two parameters that would be revealed by more data. This interaction may also depend on the rod material properties. Since our data provide only one redundant pair, little can be inferred from them. For example, there is not even consistency for the orientation component in the plane perpendicular to that containing the target normal and nominal trajectory (e.g., $\theta_D = 0$), as, for example, in Figures 34 and 35.

D. Fragment Recovery

The fragments trapped in the particle board were recovered and analyzed for the shots for which such data would be most useful. The recovery process was initiated after the witness plate-particle board packages were disassembled. Consequently, some fine particles behind the witness plate or between the particle boards may have been lost.

- Shot RS-112, S-7 Rod, 25 mm Steel Target

Sixteen steel particles ranging in mass from 0.002 to 0.5645 g were found in the particle board. For the 0.56 g

fragments to have remained in the particle board, they must have had a rather low velocity, because in other shots particles of mass similar to this nearly always perforated the particle board. This conclusion is consistent with the anomalously low fragment velocities previously noted for this shot. The mean particle mass was 0.078 g; however, the standard deviation* was 0.148 g.

- RS-113, S-7 Rod, 25 mm Steel Target

Nineteen steel fragments were found which represented about 16 percent of the witness plate perforations. About a third of the recovered particles were aluminum from the witness plate. Many of the particles which were lost apparently were between the two pieces of particle board. Sixty percent of the particles were less than 0.02 g. The large number of small particles may mean that most of the unrecovered particles were small. The mean mass fragment was 0.0345 g, and the standard deviation* was 0.0494. There was a tendency for larger fragments to be found at greater distances from the trajectory.

- RS-135, S-7 Rod, 25 mm Steel Target

This shot was a higher velocity repeat of RS-113. The sizes of the recovered particles were much smaller than from RS-113; 80 percent were less than 0.002 g. Fewer fragments were recovered because a large volume of particle board was removed near the trajectory.

- Shot RS-114, W-Alloy Rod, 25 mm Steel Target

Twenty-seven fragments were recovered. About half of these, however, were nonmagnetic, so they were presumed to be part of the witness plate (The W-Alloy was mildly magnetic). The mean mass of the fragments was 0.049 g, and the standard deviation was 0.063 g.

- RS-116, W-Alloy Rod, Steel Target

This shot was a repeat of RS-114. Fragments corresponding to 17 percent of the witness plate perforations were recovered; however, most of these were aluminum. Of the ten fragments which were not aluminum, the average weight was 0.35 g and the standard deviation was 0.028 g. Thus, the fragment distribution from the W-Alloy shots apparently did not differ significantly from that observed from the S-7 rod shots. Again, larger fragments were recovered farther from trajectory.

---

*We do not claim the distributions were Gaussian; the standard deviation merely indicates approximately how peaked the distribution was about its mean.

- RS-115, WC Rod, Steel Target

The rod fragmented on impact, and most of the particles went through the particle board and were not recovered. Of the fourteen which were found in the particle board, the average mass was 0.008 g with a standard deviation of 0.004 g. The distribution is shown in Figure 41. It seems probable that this size is characteristic of all the WC fragments; according to this interpretation, the particle board perforations were caused by large numbers of these small fragments.

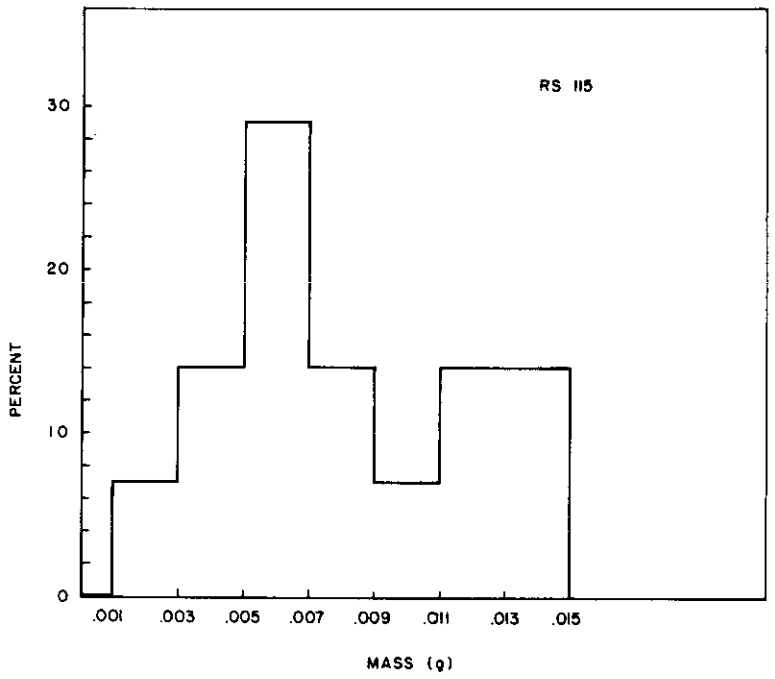

Figure 41. Distribution of recovered rod fragments found in the particle board in shot RS-115 (WC rod against 0° steel target).

- RS-130, WC Rod, Aluminum Target

All the recovered fragments from this shot were aluminum. The mean mass was 0.0009 g.

- RS-117 and RS-118, W-Alloy Rod, Oblique Steel Target

Eighteen rod and target fragments were recovered from the particle board in RS-117 and in RS-118. The two distributions are compared in Figure 42. As noted previously, the locations of the witness plate perforations of the RS-117 fragments were peripheral; and we think that the rod may have been struck by the pusher plate during penetration. The mean and standard deviations for the fragments from these two plates

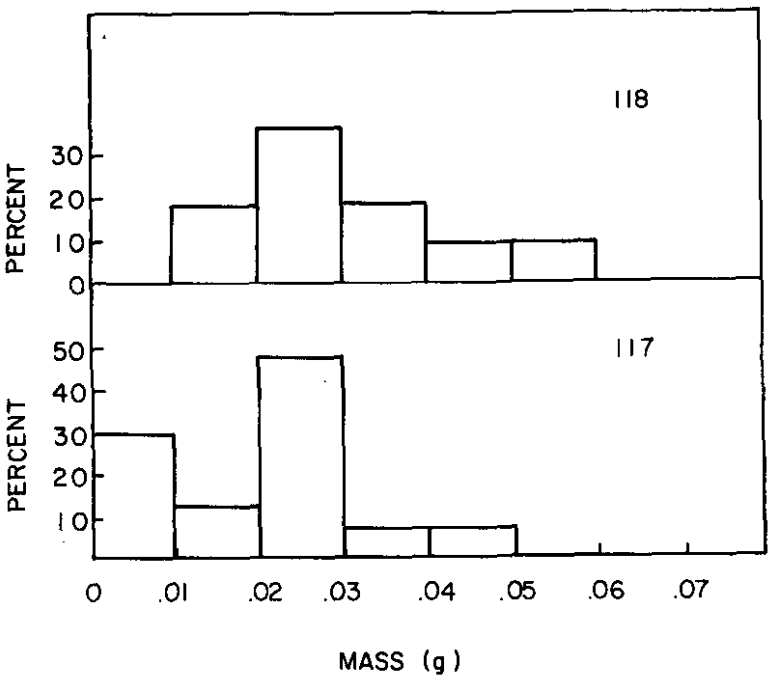

Figure 42. Comparison of distributions of rod fragments found in the particle board in shots RS-117 and RS-118.

were, respectively, 0.031 ± 0.050 g, and 0.036 ± 0.025 g. These values are essentially identical to those observed from S-7 and W-Alloy rods striking 0° obliquity targets.

In all other shots against monolithic targets, fewer than 10 rod or target fragments were recovered from the particle board. There was little value in performing additional analysis on such small populations.

Figures 43, 44, and 45 indicate integrated fragment mass distributions. These include particles which were recovered from both the wood blocks and the particle board. These data are roughly linear on the semi-log plots; this indicates that over a limited mass range, the density function (number of particles in a given mass range) is inversely proportional to the mass.

Particle size was also estimated from the holes in the witness plates. For this purpose, the curled-back edges were flattened, and the areas of the perforations were estimated. Only one quadrant, centered on the principal fragment, was examined due to the time involved in making the measurements. The results for three shots are shown in Figures 46, 47, and 48. Again, the data are roughly linear on a semi-log plot. It appears that particles of mass less than 0.002 g are usually stopped by the witness plate. Particles smaller than this were also not found in the particle board in significant quantities. If the data are fitted in the linear regions with a function of the form

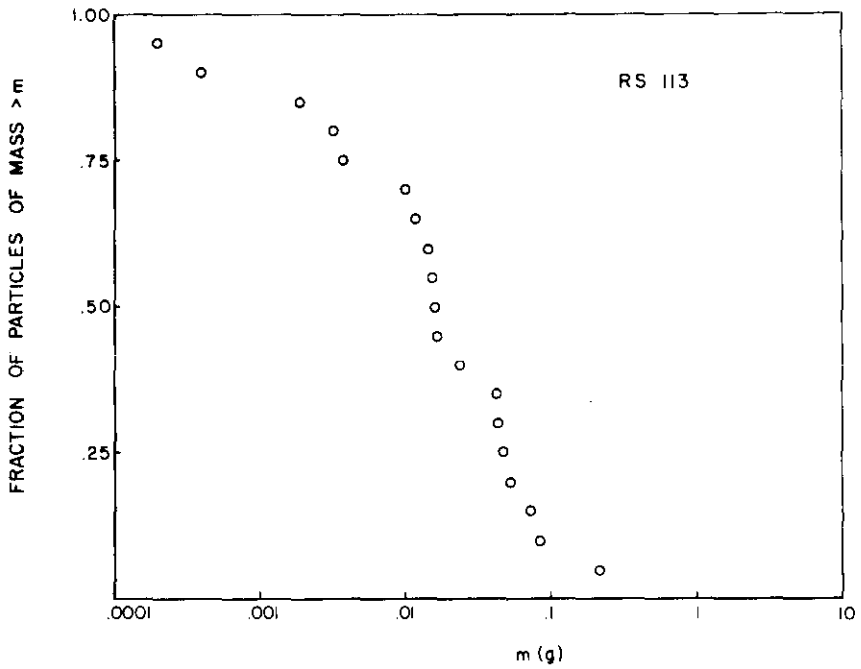

Figure 43. Integrated distribution of recovered fragments from shot RS-113, S-7 rod against a steel target. All fragments except the largest were recovered from particle board.

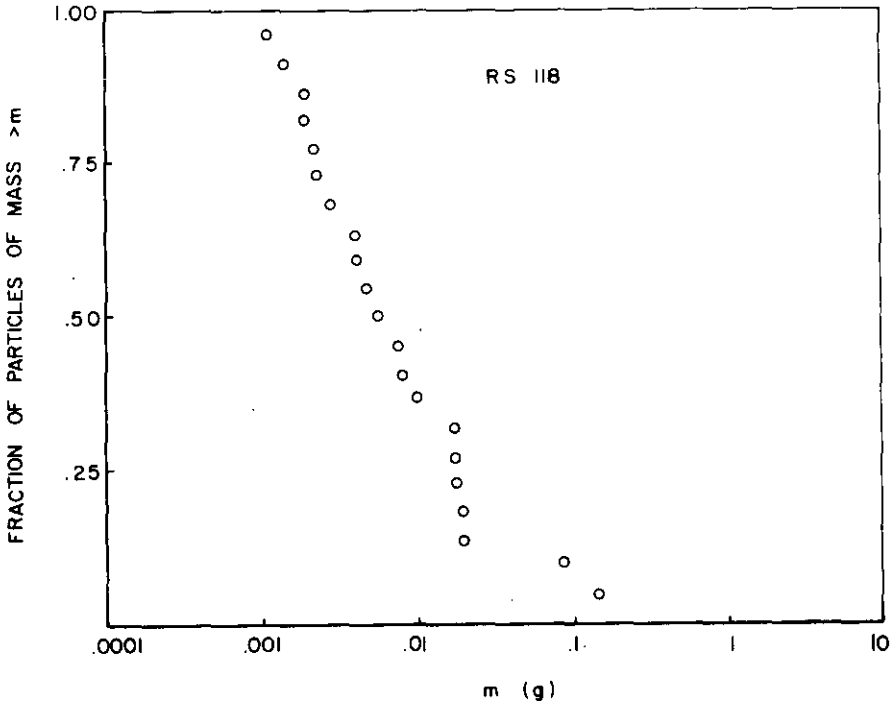

Figure 44. Integrated distribution of recovered fragments from shot RS-118 (W-Alloy rod, steel target). Particles larger than 0.01 g perforated the particle board.

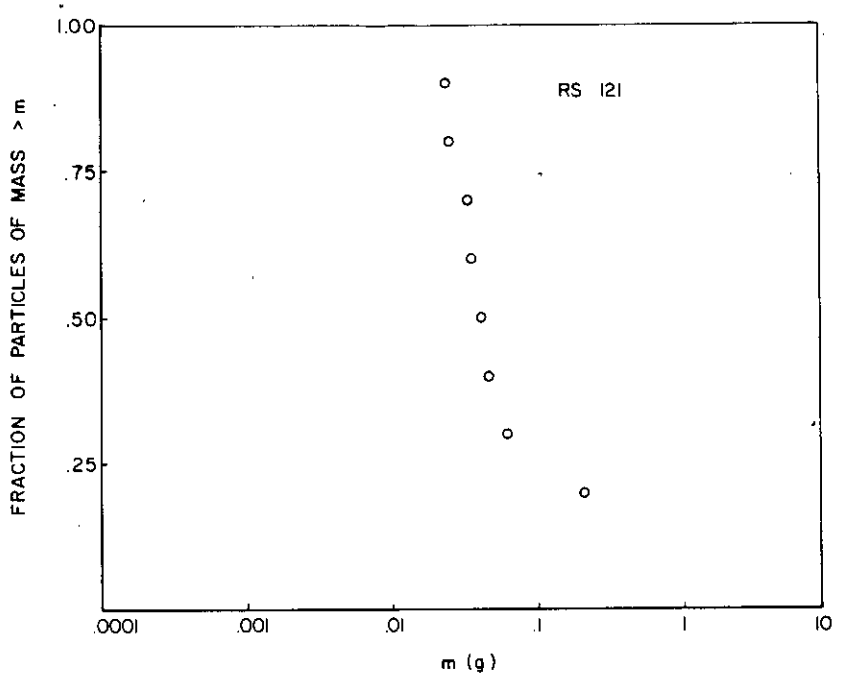

Figure 45. Integrated distribution of recovered fragments from shot RS-121, S-7 rod against oblique steel target. All but two largest are from particle board.

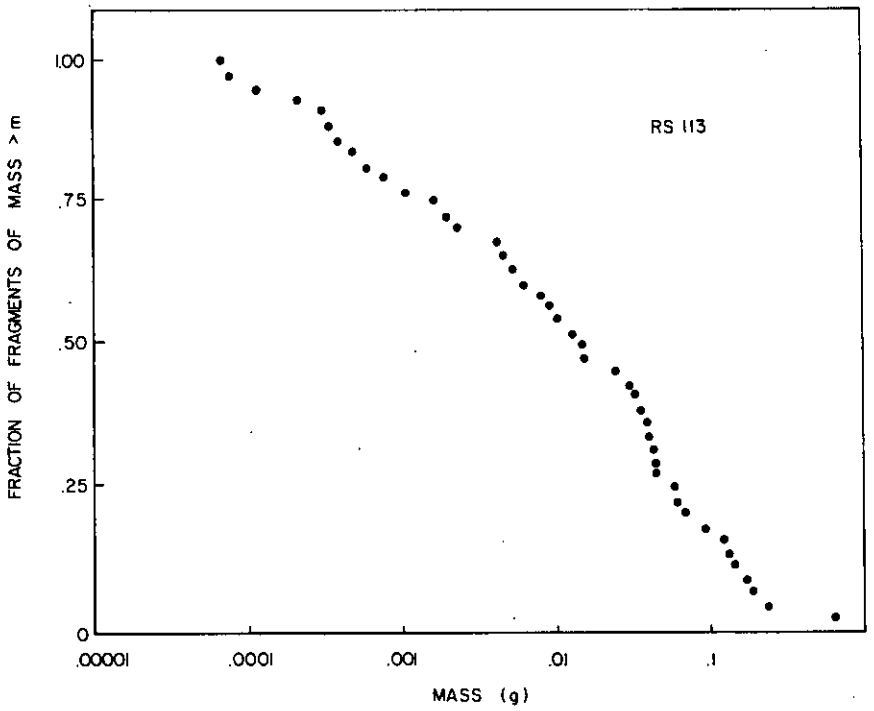

Figure 46. Integrated distribution of fragment mass in RS-113, a S-7 rod against a steel target, inferred from witness plate perforations.

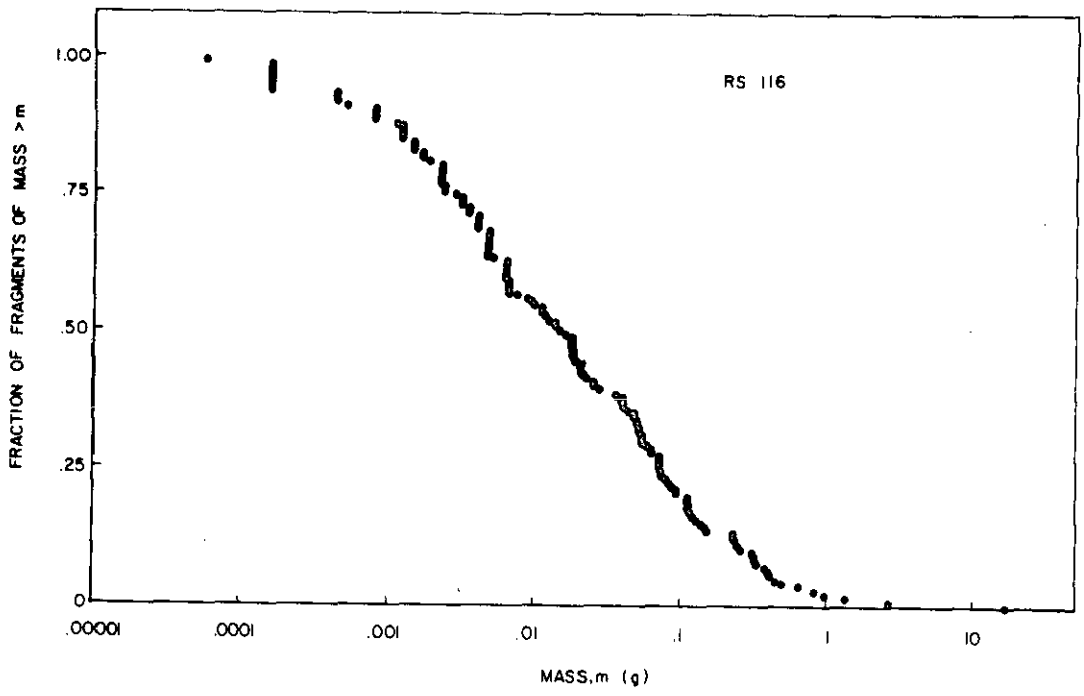

Figure 47. Integrated distribution of fragment mass from shot RS-116, W-Alloy rod against steel target, inferred from witness plate perforations. It was assumed in data reduction that all particles had W-Alloy density.

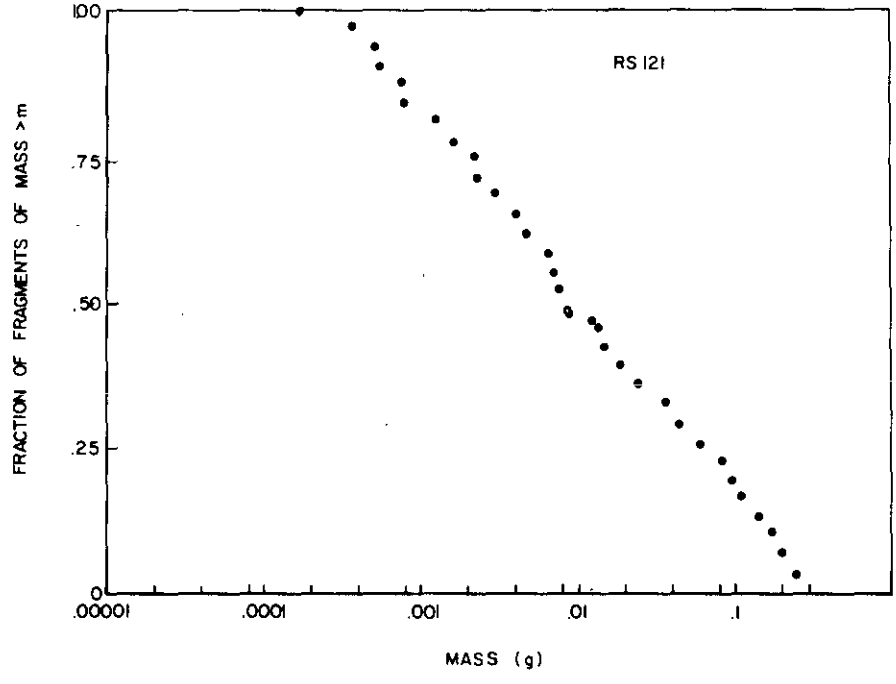

Figure 48. Integrated distribution of fragment mass from shot RS-121, S-7 rod against oblique steel target, inferred from witness plate perforations.

$$F = \frac{1}{b} \ln m + c \qquad (9)$$

where F is the fraction of particles of mass greater than m, and c is a constant, then the parameter b has the approximate values.

For RS-113	b = 10.7	for m < 0.01 g
	b = 6.1	for m > 0.01 g
For RS-116	b = 6.9	
For RS-121	b = 7.3	

The standard error in b is about ± 15 percent.

The data in Figures 46 and 48 can be compared to those of Figures 43 and 45 by considering the empirical distribution function above (Equation 9). This provides a measure of the consistency of the two methods of estimating fragment populations. If Equation (9) applies for the entire population, then a subset having mass greater than, say, m_c will have a distribution function

$$F_c(m) = \frac{\frac{-1}{b} \ln m + c}{\frac{-1}{b} \ln m_c + c} \qquad (10)$$

Equation (10) predicts a value of $\frac{\partial F_c}{\partial \ln m} = -\frac{1}{b}$ where

$$b_c = -\ln m_c + bc \qquad (11)$$

For RS-113 and 121, assuming $m_c = 0.001$ g, the righthand side of Equation (11) is equal to 5.7 for RS-113 and 5.8 for RS-121. The measured values of b_c from Figures 43 and 45 for these shots are, respectively, 5.1 and 1.6, with a ± approximately 20 percent uncertainty.

The RS-113 results suggest that the fragments sampled by the recovery process had the same distributions as those which perforated the witness plate. In Shot 121 there is a disparity. It appears that m_c for this shot may have been much larger than 0.001 g; a value of m_c of 0.05 gives 1.9, which is acceptably close to the measured value of b_c. The number of fragments recovered in RS-121 is also only a third of those of RS-113. This may be because the fragment directions were highly skewed in that shot.

E. Target Damage

All of the 4340 RC30 steel plates exhibited similar perforation morphology. A typical example is shown in Figure 49.

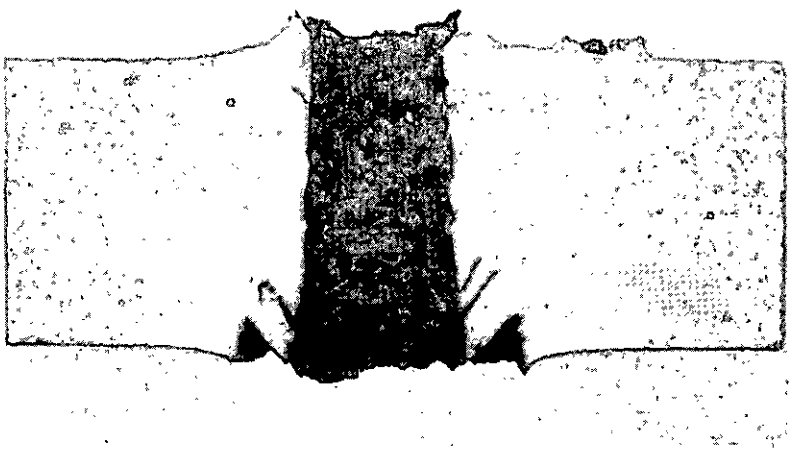

Figure 49. Cross section through perforated region of target from shot 114.

The plate has undergone spall and shear failure. Metallographic analysis of the polished cross-section reveals a ferrite-martensite structure. There are extensive deformations in the penetrated region and several thin arcs of melted material which are apparently due to adiabatic shear.

The only target which did not spall was the test plate used in RS-111. The hardness of that plate was Rockwell "B" 85, which approximately corresponds to a Rockwell "C" hardness of 3.

The smallest diameter of the perforation of the steel targets was also measured. The results are shown in Table 4.

In most cases, the diameter of the perforation increased with penetration depth. Thus, the values reported in Table 4 generally apply to the entrance region. Some trends are apparent in the data. The holes made by the W-Alloy rods were an average of 15 percent smaller in diameter than those made by S-7 rods. The smallest holes were those from the WC rods. We note that the observed trend in hole diameters is also consistent with the principle that more ductile rods make larger holes. Since the removal of material from the targets uses up kinetic energy, the rods which result in larger holes should be expected to supply less energy to behind-target fragments. Another trend evident in the table is that the smallest diameter of the holes in 45° obliquity targets was

TABLE 4. MINIMUM PERFORATION DIAMETERS

Shot Number	Rod Material	Diameter (mm)	
113	S-7	14.5	
114	W-Alloy	12.0	Normal
115	WC	9.4	Obliquity
116	W-Alloy	14.0	
135	S-7	15.7	
117	W-Alloy	10.7	
118	W-Alloy	12.5	
119	WC	13.5	45° Obliquity
120	S-7	13.0	
121	S-7	14.2	

about 10 percent smaller than that of holes in the 0° obliquity targets; this is partially due to out of roundness of the holes in the oblique targets.

IV. DISCUSSION AND ANALYSIS

A. Particle Board Fragment Discrimination

Two particle board densities were used as discriminators in fragment analysis, 0.70 and 0.75 ± 0.3 g/cm^3. BRL uses a cane fiber board which is lighter than these. The Air Force has also used a lighter particle board for fragment screening and has developed the relationship[26]

$$V = 4535.75\ [(e^{321300\ DA/M} - 1)/4.25]^{1/2} \qquad (12)$$

which is the best-fit equation to a large set of spherical and bomb fragment data. In Equation (12), V is fragment velocity in ft/s, A is fragment presented area in ft^2, M is fragment mass in mg, and D is penetration depth in inches. The particle board which the Air Force used had a density of 16-18 lb/ft^3 (0.26-0.29 g/cm^3).

In order to make manipulation easier, this equation can be transformed to more uniform units

$$V = a\ \sqrt{e^{bDA/M} - 1} \qquad (13)$$

where

$$a = 670.3\ \text{m/s}$$
$$b = 0.136\ \text{g/cm}^3$$

and A, D, and M are in cgs units.

Equation (13) has the form of a Poncelet equation. The physical basis of the Poncelet equation[27] is the assumption that retarding force on a projectile, F_D, is given by

$$F_D = (c_1 + c_3 V^2)A \qquad (14)$$

---

[24]Collins, J.A., "Fiberboard Calibration for Determination of Fragment Velocities," AFATL-TR-73-193, AD-916-759L, Sept. 1973.

[27]Backman, M.E., Terminal Ballistics, NWCTP5780, Naval Weapons Center, China Lake, CA, February 1976.

thus

$$a = \sqrt{c_1/c_3}$$
$$b = 2c_3 \tag{15}$$

To first order at least, it is reasonable to assume that for a given particle board, only c_3 is affected by density. Since the stagnation pressure is linearly proportional to density, we suppose that c_3 is also linearly proportional to density. If k is the ratio of the present particle board density to that used in the Air Force studies, then we have that for the 0.75 g/cm^3 particle board the constants in Equation (13) are

$$a = 670.3\ k^{-1/2} = 405.7\ \text{m/s}$$
$$b = 0.136\ k \quad = 0.371\ \text{g/cm}^3 \tag{16}$$

To estimate what range of particles is discriminated against, assume that A and M are related as for spheres:

$$A = \left(\frac{M}{0.7523\rho}\right)^{2/3} \tag{17}$$

where ρ is fragment density; thus from Equation (13)

$$V = a\sqrt{e^{cDM^{-1/3}\rho^{-2/3}-1}} \tag{18}$$

or

$$M = \left[\frac{dD}{\ln\frac{v^2}{a^2} + 1}\right]^3 \tag{19}$$

where

$$d = c\rho^{-2/3} \tag{20}$$

and c is a numerical constant.

Equation (18) is plotted in Figure 50 with data for fragments which perforated the particle board in various experiments, as well as a few particles which were recovered from the particle

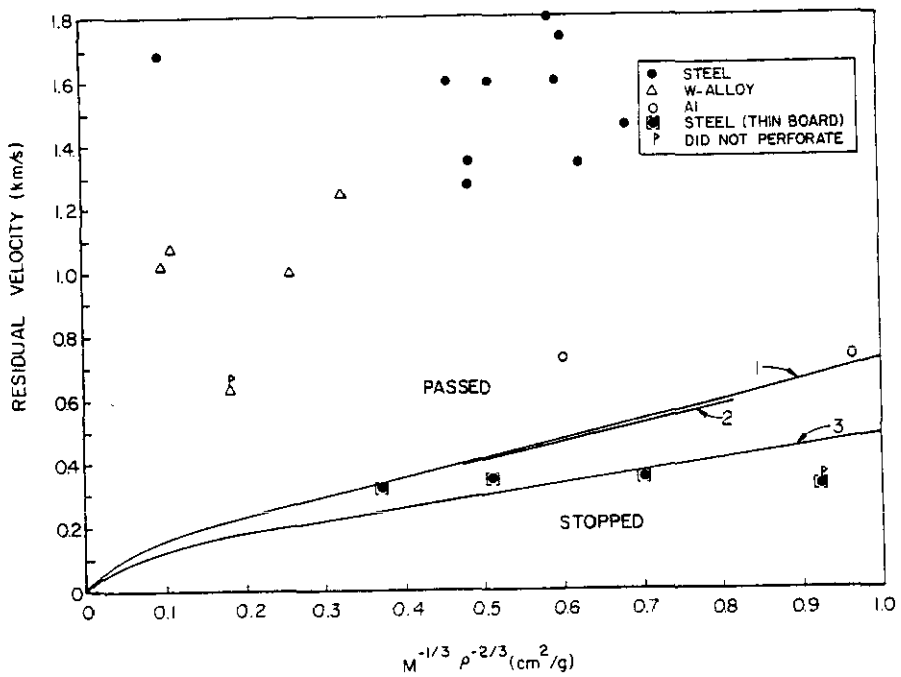

Figure 50. Penetration of fragments into particle board predicted by Equation (18). Curve 1 is for 31.8 mm, 0.75 g/cm^3 board; Curve 2 is for 31.8 mm, 0.70 g/cm^3 board; Curve 3 is for 19 mm, 0.75 g/cm board. Points show recovered fragments.

board and for which radiographic data were available. The conclusions which may be drawn from the figure are that (a) the difference between 0.70 and 0.75 g/cm particle board is not important; (b) the prediction of perforation requirements is generally consistent with the data. As pertains to the current program, the most important result is that data from shots employing the two different densities of particle board may be directly compared.

B. Fragment Size Distribution

Several formulas have been reported which describe fragment size distributions. In most cases these were derived for explosively-induced fragmentation, and it will be seen that they do not fit well the data obtained in this program.

During World War II, the following equations were developed to describe explosive case fragmentation[28]

[28]Mott, H.F., E.H. Linfoot, "A Theory of Fragmentation," A.C. 3348, Advisory Council on Scientific Research and Development (England), January 1943.

$$n = Ae^{-(m/m_o)^{1/3}} \tag{21}$$

and

$$n = \frac{B}{2m^{-1/2}} e^{-bm^{1/2}} \tag{22}$$

These equations are usually credited to Mott. In them, n(m) is the number of fragments which have mass between m and m + dm. Equation (21) can be theoretically derived from consideration of the breakup of a three-dimensional body[28,29], while Equation (22) can be derived by considering the breakup of shell which produces fragments of uniform thickness[30]. Equation (22) usually yields a better description of bomb fragment data. Note that for fragments of similar shapes, m is proportional to x^3, when x is a linear dimension of the fragment. Thus Equation (21) can be written

$$n = Ae^{-(x/x_o)} \tag{23}$$

Also, note that Equation (22) has a somewhat simpler form when written for the cumulative distribution

$$N(m) = \int_m^\infty n(m')dm' = Ce^{-cm^{1/2}} \tag{24}$$

where N(m) is the number of fragments of mass exceeding m and c is a constant. The Mott equations differ from the Rosen-Rammler law, discussed in Reference 31 for fragmentation of a hypervelocity projectile.

---

[29]Thomas, L.H., "Comments on Mott's Theory of the Fragmentation of Shells and Bombs," BRL Report No. 398, 1953. (AD #ATI 36152)

[30]Tomlinson, W.R., "Theoretical Derivation of a British Fragmentation Equation," Picatinny Arsenal Technical Report No. 1404, March 1944.

[31]Merzhievskii, L.A., V.M. Titov, "Perforation of Plates Through High-Velocity Impact," Zhornal Prikladnoi Mekhaniki i Teznicheskoi Fiziki, No. 5, pp 102-110, 1975 (translation from Plenum Publishing Corporation, 1976).

This law has the form

$$S(x) = S_o e^{-(x/x_o)^{\lambda}} \tag{25}$$

where S(x) is the sum of all the dimensions of particles of dimension larger than x, and x_o and λ are empirically-derived parameters.

To see how this differs from the Mott equations (22) and (23), consider the distribution function, n(m), implied by Equation (25):

$$S(x) = \int_x^{\infty} s'n(x')dx' \tag{26}$$

$$\frac{dS}{dx} = -xn \tag{27}$$

$$n(x) = -\frac{1}{x}\frac{dS}{dx} = \frac{S_o\lambda}{xx_o} e^{-(x/x_o)^{\lambda}} \tag{28}$$

or

$$n(m) = \frac{S_o\lambda}{x_o m^{1/3}} e^{-(m/m_o)^{\lambda/3}} \tag{29}$$

None of the above formulas resemble that derived in Chapter 2, as descriptive of our data, namely

$$F = \frac{1}{b} \ell n \ (m_o/m) \tag{30}$$

where F is the fraction of particles of mass larger than m. In order to derive n(x) from Equation (30), consider that the total number of particles is N_T. The distribution function is given by

$$n(x) = N_T \frac{dF}{dx} \tag{31}$$

$$= \frac{m_o N_T}{bm} \frac{dm}{dx} \tag{32}$$

$$= \frac{3N_T m}{bx} \qquad (33)$$

for m proportional to x^3. This is qualitatively a very different distribution than those previously discussed. Comparatively many more large fragments are predicted by our empirical formula. This may be due to the tough nature of the materials involved.

Held and Kuhl[32] developed the following fragmentation formula

$$M_n = M_T[1-\exp(-Bn^{\gamma})] \qquad (34)$$

where M_n is the mass of the first heaviest n fragments, M_T is the total mass, and B and γ are parameters. Equation (34) does not convert to a closed form for n(x). Therefore, it was evaluated as suggested in Reference 32. The quantity

$$\log(\ln \frac{M_T}{M_T - M_n}) \qquad (35)$$

was plotted against

$$\log B + \gamma \log n \qquad (36)$$

Held found a straight line of slope $\gamma = 2/3$. Figure 51 shows our results. Taking into account the smoothing introduced by the double log vertical scale, the agreement must be judged poor.

In summary, the fragment distribution observed from the S-7 steel and W-alloy impacts produced many more larger fragments than would be predicted from standard fragmentation formulas. The reasons for this result may be as follows: (1) the extreme toughness of the penetrator prevents brittle failures which are associated with most bomb casings, (2) many more smaller particles may have been produced but screened by the witness

---

[32]Held, M., and P. Kuhl, "Consideration to the Mass Distribution of Fragments by Natural-Fragmentation Combination with Preformed Fragments," Propellants and Explosives, Volume 1, 20-23, 1976.

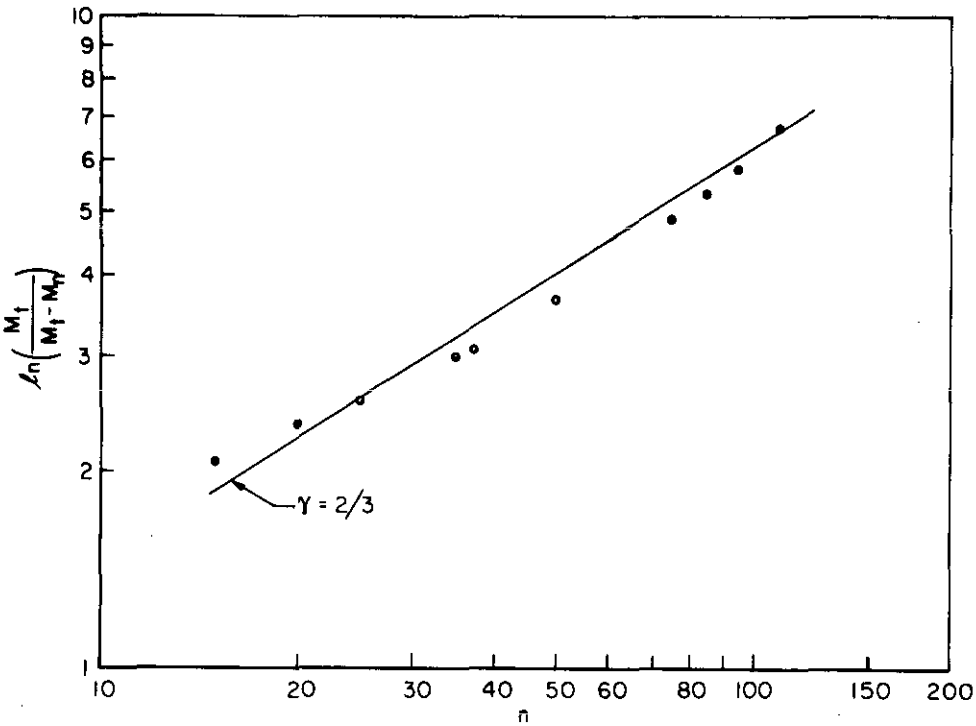

Figure 51. Fragment distribution from shot RS-116 (W-Alloy rod, 0° steel target) plotted according to Reference 30.

plates, and (3) the postulated physical processes used in deriving the Mott equation do not apply. For example, all particles do not have the same velocity; and small particles may not be derived from large particles. We believe that explanations (1) and (3) are probably the most physically significant.

c. Limit Velocities

Limit velocity values were computed for several shots using the formula

$$V_L^2 = \frac{M_s V_s^2 - \Sigma M_{Ri} V_{Ri}^2}{M_s} \qquad (37)$$

in which these symbols have their usual meanings, and the summation is over all the particles which perforated the particle board. V_L computed from Equation (37) is essentially a measure of the energy lost by the projectile during the penetration. The calculated values are shown in Table 5. Limit velocities for WC rods are not reported because there were no principal fragments. It appears from the table that the W-alloy is a slightly more effective penetrator than the S-7 steel.

TABLE 5. CALCULATIONS OF V_L

Penetrator	Target	Obliquity	V_L Predicted Using 37 (km/s)	V_L Using Method in Refs. 4 & 5†
W-Alloy	Steel Plate	0	1.22	0.9
S-7	Steel Plate	0	1.37	1.1
W-Alloy	Steel Plate	45°	1.63	1.1
S-7	Steel Plate	45°	1.76	1.3
W-Alloy	Four Al Plates	0	0.76*	

* Assuming $M_R = M_S$

† See text

Limit velocities were also derived from BRL data reported in References 4 and 5 for lower velocities (200-1450 m/s). In those investigations 64 g hemispherical-nosed L/D = 10 rods were employed against monolithic targets. The limit velocity, $\bar{V}_L$, defined by a plot of V_S and V_R values, was considered as a function of line-of-sight target thickness. The targets were 25.4 mm thick RHA at various angles of obliquity. RHA hardness in this thickness should be within 10 percent of the hardness of the targets we employed (RC30), and thus the hardness difference between RHA and our plates should have only a trivial affect on V_L. The rods used in the BRL work were S-7 steel at the same hardness as employed here and W2 tungsten alloy (W-2.4 Ni-Cu binder). W2 probably behaves similarly to the W-7Ni-3Fe material employed here.

If the geometry and materials are the same, the BRL results should scale to those of Table 5. Thus, a 25 g rod penetrating 25.4 mm of steel should have the same V_L as a 64 g rod penetrating 25.4 x $(64/25)^{1/3}$ mm of steel, and so forth. The V_L based on the BRL results are shown as a second column in Table 5.

The scaled values of V_L are considerably lower than those determined in this effort. Accepting the validity of scaling, there are five hypotheses which might be invoked to explain this observation:

1. The target materials in these studies were of significantly differing toughness;
2. The rods were of very different properties;
3. Rods lose from 30 to 50 percent more energy when penetrating a target at high speed than at low speed;
4. There was intrinsic scatter in the data;
5. The yaw of the rods in this program significantly degraded their performance as penetrators.

Explanation (1) is difficult to evaluate because there are no data known to us which compare RHA and 4340 (RC30) in 25 mm thicknesses. However, given the relatively small dependence of V_L on hardness noted by BRL[4], it seems unlikely to us that explanation (1) is valid. The second explanation probably has some validity. Certainly the W materials differed, although W2 is somewhat denser than the material used here and thus could be expected to perform better. The S-7 steels are nominally identical; however, noticeable differences in the ballistic performances of various batches of this material have been observed[23]. Nevertheless, it is unlikely that more than a minor fraction of the discrepancies detailed in Table 5 are due to this cause. Explanation (3) is difficult to refute at present, since no other data are available. The increased energy absorbed during high-velocity penetration may be associated with increases in the volume of target and penetrator material fragmented. The scatter in these types of data (explanation 4) may be evaluated, for example, from the data base provided in Reference 10, which data are fit to the equation

$$V_R = \alpha(V_s^p - V_L^p)^{1/p}. \qquad (38)$$

For L/D = 10 S-7 rods, the data vary such that in five sets of experiments the average value of p was 2.56 with a standard deviation of 0.38, or 15 percent. Examination of individual data sets suggests that for a given geometry, V_L may vary by about 10 percent. These variations are not enough to account for the trends of Table 5. Explanation (5), yaw, may indeed be a significant contributor to the V_L discrepancy pertaining to oblique targets. Yaw was only about 1° for the two 0° obliquity shots in the table. For the W-Alloy 45° obliquity shot, it was 12°; and it was not measured for the other 45° obliquity case. Thus, the two cases which show the most striking V_L discrepancy were those in which yaw is known to have, or possibly have, occurred.

In summary, these data indicate that (1) penetration efficiency decreases with velocity for those materials, and (2) the data base is not large enough to quantify this effect.

D. Comparisons of Penetrator Materials

In this section we apply the preceding data and discussion to the identification of the advantages of each of the three penetrator materials, S-7 steel, W-Alloy, and cemented WC. We discuss four areas separately: launchability, limit velocity, fragment formation from steel targets; and fragment formation from aluminum targets.

Regarding launchability, the S-7 material was found to be somewhat easier to launch, especially at higher velocities. At 600 g powder load, if we score 1 for a good launch, 0.5 for a flawed launch, and 0 for a failure, the normalized scores for the materials are S-7, 0.5 (7 shots); W-Alloy, 0.57 (7 shots); and WC, 0.63 (4 shots). Above 700 g, the score changes to S-7, 0.5 (out of 4 shots); W-Alloy, 0.0 (out of 3 shots). The low density and the relatively large diameter of an S-7 rod is probably responsible for its relatively good launchability.

Regarding limit velocity, only the S-7 and W-Alloy rods can be compared. (The disintegration of the WC rods made calculation of residual energy impossible.) It is clear from the data of Table 5 that the limit velocities against steel targets are lower for W-Alloy than for S-7 rods. This is consistent with data from previous programs, namely, dense W-Alloy rods from steel targets. The principal fragment data obtained in this program do not provide a basis for selection of W-Alloy over S-7 steel penetrators. Shots 113 and 116 can be used to compare these two materials against 25 mm 4340 steel plates at normal obliquity. The residual masses and velocities differed by less than the measured uncertainties. The same result occurs when shot 121 is compared with 118, these shots were against 45° 4340 steel plates. On the other hand, the penetrator fragment characteristics of these two materials do differ significantly. In shots 113, 120, and 121 involving S-7 rods, there were four or less perforations of the 32 mm thick particle board. In shots 116 and 118, which involved W-Alloy rods, there were 6 to 10 perforations. Under similar conditions, the W-Alloy rods produce more perforated witness plate areas than do the S-7 rods, further substantiating this observation. Based on this evidence, the fragments from the W-Alloy rods appear to be slightly more lethal. The WC rods,in contrast to the S-7 and W-Alloy ones, always disintegrated on impact. The cloud of debris typically covered a solid angle 0.5 steradians.

The above observations also apply to the aluminum targets. However, in that case the extensive fragmentation of the WC rods may provide maximum overall lethality against such targets.

The present results must be judged as preliminary because there are not enough redundant data to allow statistical analysis. It is difficult to assess the reproducibility of these results, because shots were repeated only when incomplete data were obtained or the launch package failed. Two pairs of

shots which do appear somewhat comparable are 117 and 118 (R6), and 120 and 121 (R4). The results of 117 and 118 differ markedly; in one case the fragments are small and at high departure angles, and in the other they are central. However, in 117 the pusher plate had broken up. The radiographs show an intact, slightly-yawed rod surrounded by pieces of the pusher plate. These may have struck the rod during penetration and led to breakup and deflection of the fragments. In 120 and 121 the testimonies of the two witness plates are very similar.

V. CONCLUSIONS

A. Interior Ballistics Results

Launch of 25 g long rods with laboratory guns imposes severe stresses on the launch package. A concerted development effort was successful in achieving an acceptable launch package for use up to 2 km/s. However, above that velocity the failure rate was so high that we believe a separate study on launch techniques is required. Such a program should be approached several ways: improved diagnostics to determine causes of sabot failure, modification to the rod, pusher, and plastic geometries, and finite element analyses of stresses in the launch package.

The W-Alloy rods were substantially more difficult to launch to velocities exceeding 2 km/s than were the S-7 rods. This is probably a consequence of their relatively high density, as well as their being a powder metallurgy product.

B. Terminal Ballistics Results

The behind-target data in this report are not sufficiently redundant to be employed for quantitative assessment of S-7 and W-Alloy penetrator performance. However, several important qualitative conclusions can be supported.

The fragment distributions differed markedly from those noted previously for bomb fragments and hypervelocity projectile breakup. The size distribution function from W-Alloy and S-7 impacts were inversely proportional to fragment dimension. The WC fragments were all about the same mass, namely 1 mg.

In general, the principal fragment directions did not correlate well with rod yaw or target obliquity. It appears that for tough penetrators, principal fragment direction and yaw direction are negatively correlated.

Almost all the recovered fragments derived from the penetrator. Although target spall always occurred, target fragments are apparently launched at relatively low velocities, and are overtaken almost immediately by the penetrator fragments.

The energy contained in the fragments was somewhat less for S-7 impacts than the W-Alloy impacts. The W-Alloy rods also removed less target material. It appears, therefore, that these rods are more efficient penetrators than the S-7 rods.

The limit velocities inferred from these data are greater than those found in previous lower velocity studies. There are several factors which could have contributed, but it appears that this discrepancy must be at least partially

attributed to a decrease in penetrator efficiency with increase in impact velocity.

The W-Alloy rods remained intact after penetrating four 6.35 mm aluminum plates. This is probably not a desirable property for an anti-aircraft projectile. The total fragmentation of the WC rod may make it more useful for this purpose.

The fragment stopping ability of the particle board used in this program could be successfully inferred from previous data on less-dense material.

APPENDIX A

Description of W-Ni-Fe Alloy

Provided by Mr. Graham Silsby at BRL

Inspection Prior to Final Machining

These projectiles were made from the butt end of a billet of a sintered tungsten-7 percent nickel-3 percent iron alloy produced by the ERDA Oak Ridge Y-12 Plant. This powder metallurgy product was strengthened by swaging to reduce the area 25 percent and machined to a diameter of 1-3/4 inches. This was used to produce penetrator cores used in a full scale firing program. The billet end used was selected from those available, based on good performance of the full scale round made from this billet and the availability of documentation of the material. The one selected was identified by Y-12s ID No. 7187-88-1477 on their materials fabrication certificate. It was used to produce Item 09 in 1974, subsequently fired in the full scale program.

The selected billet was radiographed by Aberdeen Proving Ground Material Test Directorate (MTD), Non-Destructive Test Section, for major flaws on two axes, with negative results, then slab cut into flat pieces. The central piece of this was given a fluorescent magnetic particle inspection by MTD with a few minor flaws visible, and then all the slabs were cut into square bars and lathe turned to final diameter. These were then inspected for flaws by Graham Silsby, Terminal Ballistics Division, Ballistic Research Laboratory, using Zyglo ZL-22 fluorescent dye penetrant, with ZP-9 formula B developer, under a Magnaflux Model ZB-26 fluorescent lamp. Parts were wiped clean of penetrant in C.P. Methanol on cotton lab wipes prior to application of the developer.

There were two finished diameters machined from the billet. There was some transverse cracking evident in a few specimens, as well as some extensive areas of porosity. In general, in the large bars, patterns of isolated pores were detected lying more or less along a single line parallel to the billet axis, while the small bars showed more scattered porosity including extensive areas of porosity and isolated pores scattered throughout the bar. Porosity was judged to be unacceptable if many pores lay in close proximity, so as to simulate cracking under flexure, and consisted of large pores as evidenced by persistance of dye penetrant under repeated wipings. Only a few areas were judged unacceptable. Porosity of the rods was called heavy if there was extensive porosity without it being

connected. Light porosity indicates pores scattered over a larger area or single pores scattered widely. Bars (with no pores were reported sound. The final machining was performed in such a fashion as to minimize unacceptable areas and/or leave them away from the middle of the rod, preferably in the front. The noses of the rods were selected to be toward the end of the billet on the assumption that this area would be more porous; this did not prove to be the case. On one projectile (No. 15) the nose was reversed to eliminate extensive porosity on what was the tail end. The finished machined rods were forwarded to the contractor for reinspection and use.

DISTRIBUTION LIST

No. of Copies	Organization
12	Commander Defense Documentation Center ATTN: DDC-DDA Cameron Station Alexandria, VA 22314
1	Director Defense Advanced Research Projects Agency ATTN: Tech. Info. 1400 Wilson Boulevard Arlington, VA 22209
1	Commander US Army Materiel Development and Readiness Command ATTN: DRCDMD-ST 5001 Eisenhower Avenue Alexandria, VA 22333
2	Commander US Army Materiel Development and Readiness Command ATTN: DRCRD-W (J. Corrigan) 5001 Eisenhower Avenue Alexandria, VA 22333
1	Commander US Army Aviation Research and Development Command ATTN: DRSAV-E 12th and Spruce Streets St. Louis, MO 63166
1	Director Us Army Air Mobility Research and Development Laboratory Ames Research Center Moffett Field, CA 94035
1	Commander US Army Electronics Research and Development Command Technical Support Activity ATTN: DELSD-L Fort Monmouth, NJ 07703
1	Commander US Army Communications Research and Development Command ATTN: DRDCO-PPA-SA Fort Monmouth, NJ 07703
3	Commander US Army Missile Research and Development Command ATTN: DRDMI-YDL DRDMI-R DRDMI-RBL Redstone Arsenal, AL 35809
1	Commander US Army Tank-Automotive Research and Development Command ATTN: DRDTA-UL Warren, MI 48090
4	Commander US Army Armament Research and Development Command ATTN: Mr. V. Guadagno Mr. R. Davitt Dr. J. T. Frasier G. Demitrak Dover, NJ 07801
2	Commander US Army Armament Research and Development Command ATTN: DRDAR-TSS (2 cys) Dover, NJ 07801
1	Commander US Army Armament Materiel Readiness Command ATTN: DRSAR-LEP-L, Tech Lib Rock Island, IL 61299

DISTRIBUTION LIST

No. of Copies	Organization
5	Commander US Army Materials and Mechanics Research Center ATTN: DRXMR-T, Mr. J. Bluhm DRXMR-T, Dr. D. Roylance DRXMR-T, Dr. A. F. Wilde3 Dr. J. Mescall DRXMR-ATL Watertown, MA 02172
1	Director US Army TRADOC Systems Analysis Activity ATTN: ATAA-SL (Tech Lib) White Sands Missile Range NM 88002
1	Deputy Assistant Secretary of the Army (R&D) Department of the Army Washington, DC 20310
1	HQDA (DAMA-ARP) WASH DC 20310
1	HQDA (DAMA-MS) WASH DC 20310
1	Commander US Army Research Office ATTN: Dr. E. Saibel PO Box 1211 Research Triangle Park NC 27709
1	Commander US Army BMD Advanced Technology Center ATTN: BMDATC-M Mr. P. Boyd PO Box 1500 Huntsville, AL 35807
1	Office of Naval Research Department of the Navy ATTN: Code ONR 439, N. Peronne 800 North Quincy Street Arlington, VA 22217
3	Commander Naval Air Systems Command ATTN: AIR-604 Washington, DC 20310
	Commander Naval Ordance Systems Command ATTN: ORD-9132 Washington, DC 20360
2	Commander Naval Air Development Center, Johnsville Warminster, PA 18974
1	Commander Naval Missile Center Point Mugu, CA 93041
1	Commander & Director David W. Taylor Naval Ship Research & Development Center Bethesda, MD 20910
2	Commander Naval Surface Weapons Center Silver Spring, MD 20910
1	Commander Naval Surface Weapons Center ATTN: Code TX, Dr. W. G. Soper Dahlgren, VA 22448
1	Commander Naval Weapons Center ATTN: Code 4057 Code 5114, Dr. E. Lundstrom Code 3813, Mr. M. Backman China Lake, CA 93555

DISTRIBUTION LIST

No. of Copies	Organization
4	Commander Naval Research Laboratory ATTN: Mr. W. J. Ferguson Dr. C. Sanday Dr. H. Pusey Dr. F. Rosenthal Washington, DC 20375
1	Superintendent Naval Postgraduate School ATTN: Dir Lib Monterey, CA 93940
2	ADTC/DLJW (MAJ D. Matuska/ LTC J. Osborn) Elign AFB, FL 32542
1	AFFDL/FES (W.H. Hackenberger) Bldg. 4F Wright-Patterson AFB, OH 45433
1	AFML/LLN (Dr. T. Nicholas) Wright-Patterson AFB, OH 45433
3	ASD (XRHD, Gerald Bennett; ENFTV M. Lentz) Wright-Patterson AFB, OH 45433
3	Director Lawrence Livermore Laboratory PO Box 808 ATTN: Dr. R. H. Toland, L-424 Dr. M. L. Wilkins Dr. R. Werne Livermore, CA 94550
1	Director Jet Propulsion Laboratory ATTN: Lib (TD) 4800 Oak Grove Drive Pasadena, CA 91103

No. of Copies	Organization
1	Headquaters National Aeronautics and Space Administration Washington, DC 20546
4	Director National Aeronautics and Space Administration Langley Research Center Langley Station Hampton, VA 23365
1	Director National Aeronautics and Space Administration Manned Spacecraft Center ATTN: Lib Houston, TX 77058
1	Aeronautical Research Associates of Princeton, Inc. 50 Washington Road Princeton, NJ 08540
2	Aerospace Corporation 2350 E. El Segundo Blvd. ATTN: Mr. L. Rubin Mr. L. G. King El Segundo, CA 90009
1	Boeing Aerospace Company ATTN: Mr. R. G. Blaisdell (M.S. 40-25) Seattle, WA 98124
1	California Research and Technology, Inc. 6269 Variel Avenue, Suite 200 ATTN: K. Kreyenhagen Woodland Hills, CA 93167

DISTRIBUTION LIST

No. of Copies	Organization
1	Effects Technology Inc. 5383 Hollister Avenue PO Box 30400 Santa Barbara, CA 93105
1	Falcon R&D 1225 S. Huron Street ATTN: Mr. R. Miller Denver, CO 80223
2	Falcon R&D Thor Facility ATTN: Mr. D. Malick Mr. J. Wilson 696 Fairmount Avenue Baltimore, MD 21204
1	FMC Corporation Ordnance Engineering Div. San Jose, CA 95114
1	General Electric Company Armament Systems Dept. Burlington, VT 05401
1	President General Research Corporation ATTN: Lib McLean, VA 22101
1	Goodier Aerospace Corp. 1210 Massillon Rd Akron, OH 44315
1	H.P. White Laboratory Bel Air, MD 21014
3	Honeywell, Inc. Government & Aerospace Products Division ATTN: Mr. J. Blackburn Dr. G. Johnson Mr. R. Simpson 600 Second Street, NE Hopkins, MN 55343
1	Kaman Sciences Corp 1500 Garden of the Gods Rd ATTN: Dr. P. Snow Colorado Springs, CO 80933
1	Lockheed Huntsville Box 1103 ATTN: Dr. E. A. Picklesimer Huntsville, AL 35809
1	Lockheed Corporation Department 8114 ATTN: Dr. C. E. Vivian
1	Materials Research Laboratory Inc. 1 Science Road Glenwood, IL 60427
1	McDonnell-Douglas Astronautics Co 5301 Bolsa Avenue ATTN: Mail Station 21-2 Dr. J. Wall Huntington Beach, CA 92647
1	New Mexico Institute of Mining and Technology Terra Group Socorro, NM 87801
1	Pacific Technical Corp 460 Ward Drive ATTN: Dr. F. K. Feldmann Santa Barbara, CA 93105
1	Philco-Ford Corp Capistrano Test Facility San Juan Capistrano, CA 92675

DISTRIBUTION LIST

No. of Copies	Organization
2	Physics International Company ATTN: Dr. D. Orphal Dr. E. T. Moore San Leandro, CA 94577
1	Rockwell International Autonetics Missile Systems Division ATTN: Dr. M. Chawla 4300 E. 5th Avenue Columbus, OH 43216
3	Sandia Laboratories ATTN: Dr. W. Herrmann Dr. L. Bertholf Dr. J. W. Nunziato Albuquerque, NM 87115
1	Science Applications Inc 201 W. Dyer Rd (Unit B) ATTN: G. Burghart Santa Ana, CA 92707
1	Science Applications Inc 101 Continental Blvd Suite 310 El Segundo, CA 90245
2	Systems, Science and Software, Inc PO Box 1620 ATTN: Dr. R. Sedgwick Ms. L. Hageman La Jolla, CA 92038
1	US Steel Corp Research Center 125 Jamison Lane Monroeville, PA 15146
1	Drexel University Department of Mechanical Engineering ATTN: Dr. P. C. Chou 32nd and Chestnut Streets Philadelphia, PA 19104
1	Forrestall Research Center Aeronautical Engineering Laboratory University ATTN: Dr. A. Eringen Princeton, NJ 08540
3	Southwest Research Institute Department of Mechanical Sciences ATTN: Dr. U. Lindholm Dr. W. Baker Dr. P. H. Francis 8500 Culebra Road San Antonio, TX 78228
3	Stanford Research Institute 333 Ravenswood Avenue ATTN: Dr. L. Seaman Dr. D. Curran Dr. D. Shockey Menlo Park, CA 94025
2	University of Arizona Civil Engineering Department ATTN: Dr. D. A. DaDeppo Dr. R. Richard Tucson, AZ 85721
4	University of California ATTN: Dr. R. Karpp Dr. J. Dienes Dr. L. Germain Dr. B. Germain Los Alamos, NM 87545

DISTRIBUTION LIST

No. of Copies	Organization	No. of Copies	Organization

2 University of Dayton
University of Dayton Research Institute
ATTN: Dr. S. J. Bless
Ms. Judy Hecht
Dayton, OH 45405

2 University of Delaware
Department of Mechanical Engineering
ATTN: Prof. J. Vinson
Dean I. Greenfield
Newark, DE 19711

1 University of Denver
Denver Research Institute
ATTN: Mr. R. F. Recht
2390 South University Boulevard
Denver, CO 80210

Aberdeen Proving Ground

Cdr, USATECOM
ATTN: Mr. W. Pless
Mr. S. Keithley
DRSTE-TO-F
Dir, USAMSAA
ATTN: Dr. J. Sperrazza
DRXSY-MP, H. Cohen
Dir, Wpns Sys Concepts Team
Bldg. E3516, EA
ATTN: DRDAR-ACW